CHALMERS
UNIVERSITY OF TECHNOLOGY

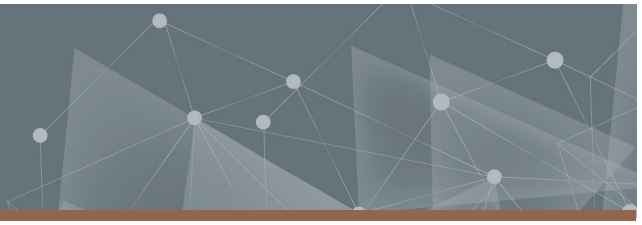

A New Way to Calibrate and Evaluate a Fuel Cell Model

Master's thesis in Physics and Applied Mechanics

SIMON JOSEFSSON, PETRONELLA TAUBE

DEPARTMENT OF ELECTRICAL ENGINEERING

CHALMERS UNIVERSITY OF TECHNOLOGY
Gothenburg, Sweden 2022
www.chalmers.se

Master's thesis 2022

A New Way to Calibrate & Evaluate a Fuel Cell Model

SIMON JOSEFSSON
PETRONELLA TAUBE

CHALMERS
UNIVERSITY OF TECHNOLOGY

Department of Electrical Engineering
Division of Electric Power Engineering
Volvo Group Trucks Technology
Chalmers University of Technology
Gothenburg, Sweden 2022

A New Way to Calibrate and Evaluate a Fuel Cell Model
SIMON JOSEFSSON, PETRONELLA TAUBE

Supervisor: Staffan Luong, Volvo Group Trucks Technology
Supervisor: Annika Carlson, RISE Research Institutes of Sweden AB
Examiner: Torbjörn Thiringer, Department of Electrical Engineering

Master's Thesis 2022
Department of Electrical Engineering
Division of Electric Power Engineering
Chalmers University of Technology
SE-412 96 Gothenburg
Telephone +46 31 772 1000

Typeset in LaTeX
Printed by Chalmers Reproservice
Gothenburg, Sweden 2022

A New Way to Calibrate and Evaluate a Fuel Cell Model
SIMON JOSEFSSON, PETRONELLA TAUBE
Department of Electrical Engineering
Chalmers University of Technology

Abstract

The increase of greenhouse gases is a constant threat to the environment. A large contributor is the transport sector. Fuel cells are said to be a possible solution for long distance heavy duty vehicles. In order to implement fuel cells into vehicles, simulation models are needed.

This thesis aims to evaluate a fuel cell component in the Gamma Technologies simulation tool GT SUITE, which is a widely used tool in industries. Additionally, this thesis aims to improve the calibration of the GT SUITE model by implementing measurements from an equivalent circuit model. The circuit model was based on electrochemical impedance spectroscopy experiments.

It was discovered that the GT SUITE model follows the behaviour of the equivalent circuit model, where the different current regions transition at the same current densities. However, it was found that the calculated ohmic resistance from the GT SUITE model was higher than what the equivalent circuit model measures. It was also found that the GT SUITE model coincides qualitatively with the literature regarding prediction of polarisation curves of other temperature states. Further work in calibrating the GT SUITE model using equivalent circuit resistances may yield improved accuracy of the ohmic resistance.

Keywords: Modelling, PEM Fuel cell, PEMFC, GT SUITE, Equivalent circuit, Impedance spectra, EIS.

Acknowledgements

This master thesis has been a pleasure and an opportunity thanks to Volvo Group. We would like to specifically thank Staffan Luong (from Volvo Group) and Annika Carlson (from RISE) for being our supervisors and always had time for discussions. They have aided us in gaining a wider understanding of fuel cell modelling and impedance spectroscopy. Similarly, we are thankful for all the Volvo employees and external experts who have helped us. Staffan Luong's coworker, Madhumita Sahoo, took time to give us insights into practical EIS laboration techniques. We would like to thank Christian Altenhofen from Gamma Technologies, for his helpful GT-SUITE simulation insights. Due to too large unforeseen delays of the planned experimental setup, Victor Shokhen and Linnea Strandberg at Chalmers University generously procured and supplied us with experimental data, on which the thesis is built on. Lastly, we would like to thank our examiner Torbjörn Thiringer, for all the feedback and inspiration.

Simon Josefsson and Petronella Taube, Gothenburg, June, 2022

Nomenclature

In this section the nomenclature used is presented to aid the reader.

Variables

A_W	Warburg coefficient [Ω $s^{-1/2}$]
C	Capacitance [F]
E^0	Thermodynamic potential between anode and cathode [V]
F	Faraday's constant [C/mol]
I	Current [A]
I_0	DC current [A]
j	Current density [A/cm^2]
j_0	Exchange current density [A/cm^2]
j_L	Limiting current density [A/cm^2]
k_{OCV}	Open circuit voltage overpotential constant [mV]
L	Inductance [H]
n	Constant phase element parameter
n_e	Number of electrons transferred in a reaction
P_W	Partial vapour pressure [Pa]
P_{sat}	Saturation pressure [Pa]
Q	Constant phase element coefficient [S s^n]
R	Universal gas constant [J/K mol]
R_{Ct}	Charge transfer resistance [Ω]
R_{ohmic}	Resistance from GT model [Ω]
R_Ω	Ohmic resistance from equivalent circuit model [Ω]
R_1	High frequency intercept [Ω]
R_2	Low frequency intercept [Ω]
r	Residual

r_{opt}	Optimisation residual
T	Temperature [K]
t_m	Electrolyte membrane thickness [cm]
V	Voltage [V]
V_{model}	Fuel cell model voltage [V]
V_{DC}	Measured DC voltage [V]
V_0	Applied DC voltage [V]
Z	Impedance [Ω]
Z_C	Capacitor impedance [Ω]
Z_L	Inductor impedance [Ω]
Z_{EIS}	Impedance from EIS data [Ω]
Z_{EC}	Impedance from equivalent circuit model [Ω]
Z_0	Impedance amplitude [Ω]

Greek

α	Charge transfer coefficient
ΔG	Gibbs free energy [J/mol]
η	Voltage loss [V]
η_{act}	Activation voltage loss [V]
η_{conc}	Concentration voltage loss [V]
η_{ohmic}	Ohmic voltage loss [V]
λ	Water content
σ	Ionic conductivity [S/cm]
σ_{11}	Ionic conductivity parameter for the membrane
σ_{12}	Ionic conductivity parameter for the membrane
σ_2	Ionic conductivity parameter for the membrane
σ_{303K}	Ionic conductivity at 303 K [S/cm]
θ	Phase shift [rad]
ω	AC wave frequency [1/s]

Abbreviations

CL Catalyst Layer. 6, 7
CPE Constant Phase Element. 14, 34–36, 38

EC Equivalent Circuit. IX, X, XIII, XIV, 12, 19, 21, 30–32, 35–39, 41
EDL Electrical Double Layer. 13–15, 32
EIS Electrochemical Impedance Spectroscopy. 11, 13, 15, 19, 21, 30, 38, 41, 42

fcaEC Flexible, constant anode EC. IX, 34–36
fcanEC Flexible, constant anode and n EC. IX, 34–36
fEC Flexible EC. 18, 30–35, 37, 38

GDL Gas Diffusion Layer. 6, 7, 23

HOR Hydrogen Oxidation Reaction. III, 5, 7, 13, 17

MEA Membrane Electrode Assembly. 5–7
MPL Microporous Layer. 6, 7

OCV Open Circuit Voltage. 8, 18, 24–26
ORR Oxygen Reduction Reaction. III, 6, 7, 17

PEM fuel cell Polymer Electrolyte Membrane Fuel Cell. 5–8, 10, 33, 42

RH Relative Humidity. VII, VIII, XI, 10, 17, 23–29, 37

TPB Triple Phase Boundary. 7, 10, 11, 13, 14, 21

Contents

1

Introduction

1.1 Background

As the world's population increases and industrialisation continues to grow, the demand for energy and the use of fossil fuels become a more prominent problem in our society [1]. Our way of living today is not sustainable for future generations. In many big cities throughout the world, there is an urgent need to decrease the emissions from transport. These emissions affect local peoples' physical health. It has come to the point that governments are restricting the use of internal combustion engine (ICE) vehicles in the largest cities [2]. Extensive research and improvement of existing technology are being made to decrease the environmental footprint from the transportation sector. In 2015, the transport sector was responsible for 24% of the global CO_2 emissions [3].

There are two main types of technologies in transport vehicles that generate power: combustion engines and electric engines. Unlike the combustion engine, electrical engines have no tailpipe emissions [4]. Electric engines are driven either by a battery or a fuel cell, where the emissions are shifted to the location where the electricity or hydrogen are being produced. Most of the hydrogen today is produced from natural gas [5]. This could be changed in the future as the world restricts the use of fossil fuels and electrolysis becomes the more economically beneficial choice.

Batteries are limited by the driving range. They have been difficult to scale between power and capacity since they are intertwined with each other. They also have the limitation of needing to be charged [6, 7]. Unlike batteries, fuel cells allow for easy independent scaling between power and capacity, since power is determined by the size of the cell and capacity is determined by the storage size of the fuel, which is independent of each other [7]. Thus, battery vehicles are more suitable for shorter distances and low cargo weight, while fuel cell vehicles are more suitable for longer distances and heavier cargo weight [4]. However, there are still many issues needed to be solved for fuel cell trucks to be commercialised on a large market. The main problem is the infrastructure of hydrogen: producing renewable hydrogen and storing it [4].

1.2 Fuel Cell Model Developments

In order to incorporate fuel cells into heavy vehicles, fuel cell models are needed to predict their behaviour. These models can be categorised as either process or measurement models [8]. Process models means resolving some governing equations, for instance the momentum and mass transport of each species and the energy transport. One of the first process models was one-dimensional, isothermal and steady state with the assumption that all water formed, was evenly dispersed [9]. Since then, transient, non-isothermal, three dimensional models with two-phase flow have been developed that require knowledge of microscopic characteristics of the porous electrodes [10]. Still, 1D and 2D models are of great interest for their low computational cost and requirements, such as fewer parameters. Measurement models also require fewer physical parameters, and offer a general overview of the fuel cell behaviour [8]. They build on impedance measurements and generate an equivalent model with electrical components that create the same impedance spectrum as a measured one [8]. Two different kinds of measurement models are usually implemented: a simplified equivalent circuit model or a complex transmission line model. One of the earliest simplified equivalent circuits was proposed by Randles et al. and has since then been modified in various ways to incorporate different complex phenomena [8, 11]. The second approach is the transmission line model. It is made up of a chain of smaller circuits, similar to a discretisation, to describe the ion transport in greater detail [8].

To validate and calibrate fuel cell models, the ordinary approach for process models is to compare polarisation curve data. This method is used for everything from 1D to 3D process models [12]. Measurement models are calibrated from EIS data [11]. Bertei et al. validated a physical solid oxide fuel cell model by verifying microscopic parameters using 3D tomography and the overall transient behaviour using impedance spectroscopy [13]. The impedance spectroscopy was also used to calibrate the model by deriving an equivalent circuit and calibrating it. The equivalent circuit parameters were fitted using an Arrhenius equation in order to make them temperature dependent and more widely applicable.

A popular simulation tool in many industries is GT SUITE. This tool has been developed by the company Gamma Technologies and has many built-in libraries of components that solve for multi-physical tasks such as problems in thermal transport, solid mechanics, flow mechanics, acoustics, electromechanics and control [14]. One of the libraries contain a fuel cell stack component, which acts as a black box. It is built on a mix of fuel cell science articles, hence it is a process model that has yet to be validated externally.

1.3 Purpose

The aim of this project is to evaluate the GT fuel cell component by comparing it with an equivalent circuit model based on experimental data, as well as to compare

polarisation curves. A second goal is to investigate if there are ways to improve the calibration method using electrochemical impedance spectroscopy and equivalent circuits.

2

Theory and Fundamentals

To create a model of a polymer electrolyte membrane (PEM) fuel cell, it is important to have a fundamental understanding about the underlying principles of the fuel cell. In the following section, the theory and fundamentals necessary will be explained.

2.1 Fuel Cells

Fuel cells are electrochemical cells that generate electrical energy by converting chemical energy of a fuel and an oxidising agent through redox reactions. This is achieved at an efficiency of 40-60 % depending on design [15], with the by-products of heat and water [16]. The main component of a fuel cell is the membrane electrode assembly (MEA), which consists of an electrolyte sandwiched between an anode and a cathode. There are different types of fuel cells and they are classified based on which electrolyte material and fuel is used. The main types of fuel cells are PEM fuel cells, solid oxide fuel cells, alkaline fuel cells, direct methanol fuel cells, phosphoric acid fuel cells and molten carbonate fuel cells. All kinds of fuel cells have the same underlying electrochemical principles, but differ in operational temperature regime, materials, fuel flexibility and performance [7]. This project focuses on PEM fuel cells; they are attractive in many applications due to their low operational temperature and higher power density of 500-2500mW/cm^2 [7]. The low operational temperature allows for relatively fast start and stop transitions of the fuel cell. This is an important property for transport vehicles and other portable applications [7]. It also decreases the requirements of heat transport from the fuel cell stack, allowing for water as a safe liquid coolant as well as lowering restrictions on heat tolerance of any surrounding materials.

PEM fuel cells run on hydrogen gas. The gas is oxidised at the anode by the following reaction

$$H_2 \longrightarrow 2H^+ + 2e^-,$$

and it is called the hydrogen oxidation reaction (HOR), which is a dissociation reaction. The produced protons are transported through the electrolyte to the cathode. The electrolyte in a PEM fuel cell is, as the name suggests, a polymer. The electrons released from the dissociation reaction are transported through an outer circuit to the cathode, which generates a current. At the cathode, the protons and electrons reacts with the oxidising agent (O_2) according to the reaction

$$\frac{1}{2}O_2 + 2H^+ + 2e^- \longrightarrow H_2O,$$

and is called the oxygen reduction reaction (ORR). The operation of a PEM fuel cell is visualised in Figure 2.1 [17].

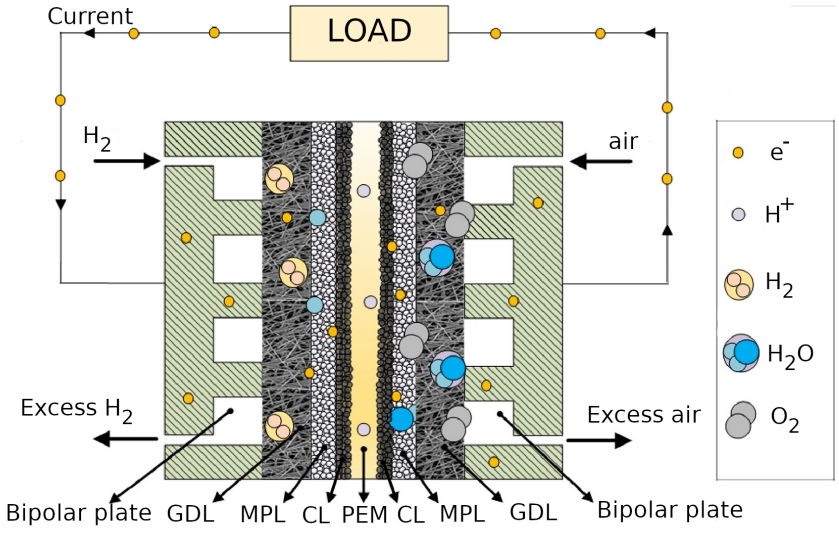

Figure 2.1: A PEM fuel cell schematic with the following abbreviations: GDL - Gas Diffusion Layer, MPL - Micro Porous Layer, CL - Catalyst Layer, PEM - Polymer Electrolyte Membrane. Hydrogen is fed at the anode (to the left of the figure) and is transported to the CL, where it split into electrons and protons. Protons travel through the membrane while electrons generate a current in the external circuit. The electrons and protons are then conducted to the CL at the cathode to react with oxygen and form water vapour. (Figure reference, altered with permission: Hao Wu (2009))

2.2 Fundamentals of the Components

In order to understand how a PEM fuel cell operates, it is important to understand the task of the different components and their limitations. The electrolyte is used to transport protons from the anode to cathode. It is required to have a high proton conductivity, be electrically insulating, as well as be mechanically and thermally stable in order to perform as intended. The most commonly used polymer membrane used is Nafion, which has been developed by DuPont [11]. Nafion has the desired properties of an electrolyte, but it is temperature and moisture sensitive. If it dries out in use, the life time is drastically shortened, and with increased humidity, the proton conductivity is greatly increased. Since the conductivity in the membrane is strongly dependent on the humidity, the operational temperature of PEM fuel cells are often limited to below 100°C, hence the ideal operational temperature of the cell is around 80 °C [11, 18].

Besides the electrolyte, the MEA also consists of an anode and a cathode. The cathode and anode need to be able to perform multiple functions, such as gas transport to the reaction sites. The electrodes consist of smaller components, namely the catalyst layer (CL), the microporous layer (MPL) and the gas diffusion layer (GDL).

The CL is required in order to lower the activation energy for the HOR and ORR, especially at the low operational temperature of a PEM fuel cell. It is sometimes only the CL and the membrane that are included in the MEA. The most commonly used catalyst in PEM fuel cell is Pt (platinum) [11, 19]. The Pt load is an important factor of PEM fuel cells as it is a scarce and expensive material. Therefore, a lot of research is focused on reducing the Pt load in the PEM fuel cell [19]. The GDL and MPL are together called the gas diffusion medium. Its function is to transport and distribute the gaseous reactants to the reaction sites and transport the water product away. The gas diffusion medium consists of a porous carbon material, where the MPL has a lower porosity than the GDL [20].[1] It also has the important property of being highly electrically conductive. In a fuel cell stack, the MEA is placed between pairs of bipolar plates that has gas flow channels which supply the electrodes with reactants. It also includes current collectors that connect to the external circuitry [11]. If a single cell is used instead of a fuel cell stack, no bipolar plates are needed as they electronically connect cells. A single fuel cell has flow field channels and current collectors without any connection to other cells.

The interface where the electrolyte, catalyst and gas diffusion medium are in contact is called the triple phase boundary (TPB) region. This is where the HOR and ORR take place [7, 19, 20]. To be able to increase the current with small losses, efficient transport to and from the TPB region is needed. This is achieved with the properties of the components already mentioned. Note that these reaction sites can be everywhere throughout the electrode as long as it has contact to the three phases (electrolyte, catalyst and gas diffusion medium).

2.3 Polarisation Curves

The performance of a fuel cell can be summarised with a graph of its current-voltage characteristic called a polarisation curve [7]. A typical polarisation curve is presented in Figure 2.2. It shows the voltage output for any given current load and the voltage would preferably be as high as possible for a specific current. Polarisation curves are often measured using a galvanostat/potentiostat, which draws a fixed current from the fuel cell and measures the output voltage or vice versa. Note that in Figure 2.2, the current is normalised against geometric area[2] of a single fuel cell, as the current produced is directly proportional to the area of the reaction interface [7].

The highest theoretical voltage created by a single H_2/O_2 fuel cell is given from the Gibbs free energy ΔG, since it is a measurement of the maximum reversible work [7, 11]. The highest potential between the electrodes, E^0 is

$$E^0 = -\frac{\Delta G}{n_e F}, \tag{2.1}$$

[1] Porosity is the percentage of void space and can also be given from 0 to 1.
[2] This is the cross sectional area that protons are transported through.

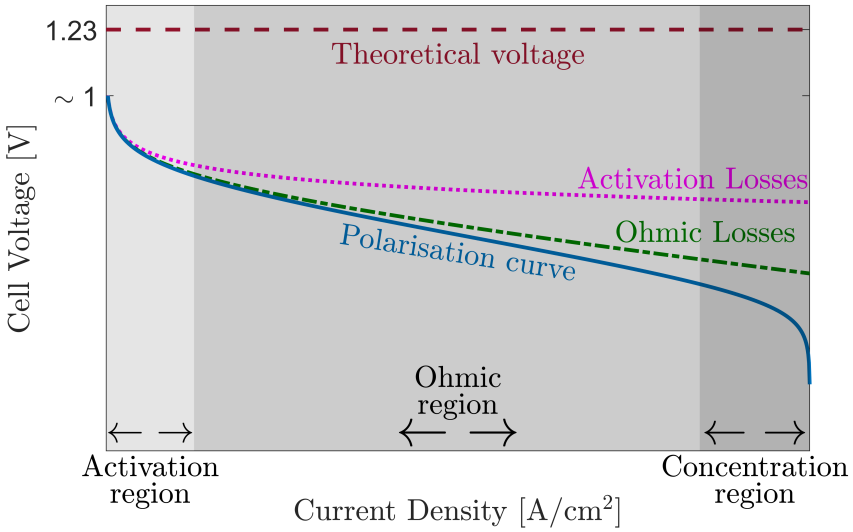

Figure 2.2: A polarisation curve of the typical behaviour of a PEM fuel cell. Three regions are indicated, activation, ohmic and mass transport. Each field indicates which voltage loss is dominating. Note that each field is transitional in reality.

where n_e is the number of electrons transferred per hydrogen gas molecule and F is the Faraday constant (C/mol electrons). The maximum theoretical potential E^0 is 1.23 V if the water produced is in vapour phase.[3]

The highest voltage is measured at no current[4] and is called the open circuit voltage (OCV). This voltage is the difference between the anode and cathode potential and ideally would have been the theoretical potential E^0, but as seen in in Figure 2.2, the actual voltage (solid line) is always lower. The decrease is caused by hydrogen gas crossing over the membrane to the cathode and then reacting with Pt and oxygen. This lowers the cathodic potential and is referred to as the hydrogen crossover loss. There are also other properties that influence the decrease in voltage such as temperature, gas pressure and the purity of oxygen. Accounting for these losses brings the OCV down to around 1 V [11]. If more than 1V is required, a stack is necessary (fuel cells in series).

As seen in Figure 2.2, the voltage decreases with increased current load. This is due to several irreversible losses that are connected to different regions of the polarisation curve. At low currents, losses are mainly connected to activation losses. These losses are related to the reaction kinetics, where reactions need a reaction overpotential in order to overcome the activation energy [7, 11]. The catalyst decreases the activation energy, thus lowering the activation loss. At intermediate currents, the ohmic losses dominate. These losses are related to charge transport of electrons and ions.

[3] n_e = 2 electrons per hydrogen gas molecule, F = 96 485.3 C/mol electrons and ΔG is -237 kJ/mol at standard conditions (25 °C, 1 atm) for water vapour.

[4] Note, no current does not mean that no reactions take place, just no net reactions (both half cell reactions are in equilibrium).

As the name suggests, they follow Ohm's law. The main contribution is typically from the ionic transport. In order to decrease the ohmic losses, thinner electrolytes can be used, keeping in mind that the mechanical strength of the electrolyte is then lowered [7]. At high currents, reactant mass transport become rate limiting due to the overall increase in reaction rate as well as opposed transport of produced water which may block the reactant gases. These losses are called concentration or mass transport losses. Ohmic losses relate to charged particle mass transport, while concentration losses are due to limiting transport of uncharged particles. In order to decrease these losses, optimal design of the electrodes and flow channels are therefore needed [7].

The losses affect all current regions, but dominate in different regions as indicated in Figure 2.2. The voltage output is the theoretical potential subtracted by the losses

$$V = E^0 - \eta_{cross} - \eta_{act} - \eta_{ohmic} - \eta_{conc}, \tag{2.2}$$

where η are the different losses related to the hydrogen crossover loss (η_{cross}), activation losses (η_{act}), ohmic losses (η_{ohmic}) and concentration losses (η_{conc}) [11]. The difference between E^0 and the measured voltage is called the overpotential and is dependent on the current load.

2.4 Losses Modelling

The three main voltage losses, activation, ohmic and concentration loss, can be further studied. The Butler-Volmer equation is one of the most fundamental equations in electrochemical kinetics. It describes the relationship between the current density and the activation overpotential. It is given as

$$j = j_0 \left(e^{\alpha n_e F \eta_{act}/(RT)} - e^{-(1-\alpha) n_e F \eta_{act}/(RT)} \right), \tag{2.3}$$

where α is the charge transfer coefficient. α describes the symmetry of the activation barrier in forward and backward direction [7, 9]. The forward activation barrier is decreased with $\alpha n F \eta_{act}$. The first term in the Butler-Volmer equation is the forward current density, while the second is the reverse. j_0 is the exchange current density, which is equal to the magnitude of the forward and reverse current density when no net current flows. R is the universal gas constant and T is the temperature in Kelvin.

The Tafel equation is a numerical simplification of the Butler-Volmer equation [7]. At low net current density ($j \ll j_0$) the current density in (2.3) can be simplified to

$$j = j_0 \frac{n_e F \eta_{act}}{RT}, \tag{2.4}$$

by Taylor series expansion to the first order ($e^x \approx 1 + x$). At high current ($j \gg j_0$), the backward reaction rate is negligible in comparison to the forward reaction

$$j = j_0 e^{\alpha n_e F \eta_{act}/(RT)}. \tag{2.5}$$

Solving for η_{act} yields the Tafel equation

$$\eta_{act} = \frac{RT}{n_e F}\frac{j}{j_0}, \quad j \ll j_0, \tag{2.6}$$

$$\eta_{act} = \frac{RT}{\alpha n_e F}(\ln j - \ln j_0), \quad j \gg j_0. \tag{2.7}$$

Note that the Tafel equation is required to be continuous, thus the gap between 2.6 and 2.7 has to be small.

Next, the ohmic losses are given as

$$\eta_{ohm} = jR_{ohmic}, \tag{2.8}$$

where R_{ohmic} is the total resistance of the fuel cell (with unit Ωcm^2 here), which is dependent on material properties of the electrodes, the membrane, as well as its humidity. One empirical formula that can be used for Nafion membranes is to integrate over the membrane thickness t_m [7, 9]

$$R_{ohmic} = \int_0^{t_m} \frac{dz}{\sigma(z)} \approx \frac{t_m}{\sigma}, \tag{2.9}$$

$$\sigma(T, \lambda) = \sigma_{303K}(\lambda)\left(\sigma_2(\frac{1}{303} - \frac{1}{T})\right), \tag{2.10}$$

$$\sigma_{303K}(\lambda) = \sigma_{11}\lambda - \sigma_{12}, \tag{2.11}$$

where σ is the conductivity with the units $\Omega^{-1}cm^{-1}$ (σ_{303K} is at 303 Kelvin), and σ_{11}, σ_{12} and σ_2 are Nafion membrane parameters. λ is the water content of the membrane, and is found through empirical functions of relative humidity (also called vapour activity) of the membrane [7, 9]. The water content is defined as the number of water molecules per charged Nafion polymer site (R - SO_3^-) and reaches 14 at 100% relative humidity. The relative humidity (RH) of the membrane is

$$RH = \frac{P_W}{P_{sat}}, \tag{2.12}$$

where P_W is the water vapour partial pressure and P_{sat} is the saturation pressure of water in air [7, 9].

Lastly, the mass transport losses are modelled using the following empirical formula

$$\eta_{conc} = \frac{RT}{n_e F}\ln\frac{j_L}{j_L - j}, \tag{2.13}$$

where j_L is the limiting current density, the necessary current density to deplete the reactant concentration at the TPB [7, 9].

2.5 Starvation

A PEM fuel cell that is operated at high currents reaches a tipping point where the voltage quickly drops, as shown in Figure 2.2 in the concentration region. At

that point, the fuel cell is suffering from starvation of reactants. The reaction sites are not supplied with enough reactants to generate the required current. Starvation can occur when the cell is fed inlet gases with low reactant stoichiometric ratios (normal operation: stoichiometric ratio of 1.3 and 1.5 for H_2 and O_2 respectively at 2-3 bar [18]) or when excess water blocks routes to the reaction sites (i.e. flooding) [21]. Water production at the cathode is proportional to the current density. For a constant reactant flow rate over the polarisation curve, the risk of starvation is greatest at high currents.

Operating a fuel cell at starvation conditions leads to material degradation of the cell. As the preferred reactant becomes unavailable at the electrodes, the local potential increases which allows for side reactions. The electrodes may then suffer from local carbon corrosion, where the carbon is oxidised and the Pt catalyst loses its carrying structure. The loose Pt may then lump together to other Pt particles, dissolve into the ionomer, or exit the fuel cell [22, 23]. Furthermore, if the anode side is starved, water may react at the anode TPB to form protons, electrons and oxygen gas [24]. With high enough built up local potential, the Pt catalyst may react with the oxygen to form oxides, thus removing it as a possible reaction site permanently. If the cathode is starved, the protons and electrons at the cathode TPB reforms into hydrogen. No matter which reactant is limited, it can lead to an explosive hydrogen and oxygen gas mix [24].

2.6 Electrochemical Impedance Spectroscopy

While polarisation curves are great for representing the fuel cell performance at a specific state (pressure, temperature, humidity, concentration), it is not apparent what phenomena lowers or increases performance. The electrochemical impedance spectroscopy (EIS) has the ability to differentiate loss contributions from different processes in the fuel cell, because it is a time resolved technique and the different processes occur at different rates. However, it is generally more difficult to analyse and measure than a polarisation curve [7, 11, 25].

EIS is a method to measure the response of an electrical system by exposing it to a weak sinusoidal AC current or voltage with varying frequencies. The fuel cell is an electrochemical system that consists of many processes such as charge transfer, mass transfer and adsorption of species. These processes have certain delays and losses that can be interpreted as the impedance of electrical components in a circuit. By imposing an AC voltage onto the circuit, the impedance Z is given as

$$Z = \frac{V(t)}{I(t)} = \frac{V_0 e^{i\omega t}}{I_0 e^{i\omega t - i\phi}} = Z_0 e^{i\phi} = Z_0(cos(\phi) + isin(\phi)), \tag{2.14}$$

with the amplitude voltage V_0, current I_0 and frequency ω. The produced current may have a phase shift ϕ depending on the behaviour of the fuel cell components [11].

2.6.1 Electrical Component Impedance Responses

Electrical components have different impedance responses. A component that only responds with a real valued impedance is a resistor (the phase shift is zero). A capacitor and an inductor has the following impedances

$$Z_C(\omega) = \frac{1}{i\omega C}, \tag{2.15}$$

$$Z_L(\omega) = i\omega L, \tag{2.16}$$

where C and L are the capacitance and inductance. The responses of the corresponding components are presented as Nyquist curves in Figure 2.3**a**. A Nyquist curve is the imaginary and real part of the impedance plotted against each other as the AC frequency is varied.

2.6.2 Equivalent Circuit for a Fuel Cell

One common way of modelling a fuel cell is to make an equivalent circuit (EC) model, where the circuit produces the same response as the electrochemical cell. The model should be as simple as possible to represent the processes in the fuel cell [11]. Commonly, many processes are described by one component. These equivalent circuit models are a way of extracting information about the reaction kinetics, ohmic conduction, mass transport and other processes [7]. Note that the electrical circuits used to describe a system is not unique and it can be difficult to pinpoint the exact physical origin of the impedance [8, 26].

The most common equivalent circuit model is the Randles circuit. It includes a resistor, R_Ω followed by a parallel resistor and capacitor (R_{Ct}/C) [11]. The total impedance of the Randles circuit is

$$Z(\omega) = R_\Omega + \frac{1}{\frac{1}{R_{Ct}} + i\omega C}, \tag{2.17}$$

and the response of this equivalent circuit is shown in Figure 2.3**b**, together with its circuit diagram. For high frequencies, the impedance tends towards R_Ω and for low frequencies toward $R_\Omega + R_{Ct}$. The Randles circuit is both useful as a model and can serve as a starting point in the equivalent circuit modelling, where more electrical components can be added to represent different physical behaviours and make a better fit to the EIS data.

The resistor R_Ω in the Randles circuit represent the ohmic losses, which come from the various cell components and the contact resistance between them. The main contributor to variations in R_Ω is the membrane electrolyte, due to shifts in membrane hydration (which modifies the ionic resistivity) [11, 27, 28]. The reaction process is overall more complex at the cathode than the anode, as well as being slower, thus the impedance from EIS mainly resembles the behaviour of the cathode [11, 28]. Therefore, the parallel circuit in the Randles circuit mainly correspond to

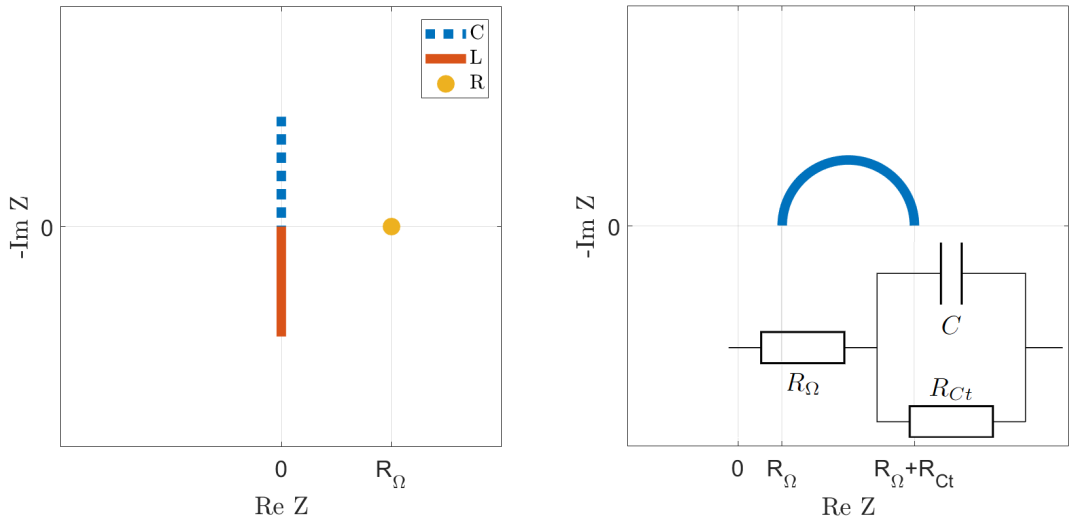

(a) **(b)**

Figure 2.3: Nyquist curve for **(a)** a capacitor, inductor and resistor and **(b)** Randles circuit response with corresponding circuit. The resistance R_Ω is the displacement along the real impedance axis.

the cathodic processes. The resistance, R_{Ct}, corresponds to the response from the charge transfer and the capacitance, C, corresponds to the response of the electrical double layer (EDL). The charge transfer is the transport of electrons between the electrode and the TPB [7, 11]. The EDL is developed on the interface between the electrode/electrolyte and is extremely thin [11]. The EDL is the distribution of mobile charges close to a charged interface. As the name suggests, roughly two layers form. The layer closest to the surface consist of adsorbed ions and the layer further away consist of ions attracted by columbic forces [29].

The ideal EIS response of a fuel cell is visualised in Figure 2.4 for the different current regions (activation, ohmic and mass transfer) [7]. $R1$ represents the high frequency intercept and is modelled as R_Ω in the Randles circuit. $R2$ is the low frequency intercept and is the total resistance of the fuel cell, which is the negative slope of the polarisation curve [11]. In the activation region, two semicircles are typically seen as indicated in Figure 2.4**a**. One is often smaller or indistinguishable from the second larger semicircle. The small semicircle to the left is commonly interpreted as being related to the anodic behaviour. This is since the HOR occurs at a higher rate. It is therefore in the high frequency region. In order to model the anodic response in an equivalent circuit, an additional parallel circuit can be added to the Randles circuit. For higher current, the semicircles decrease in size [30] as seen in Figure 2.4**b**.

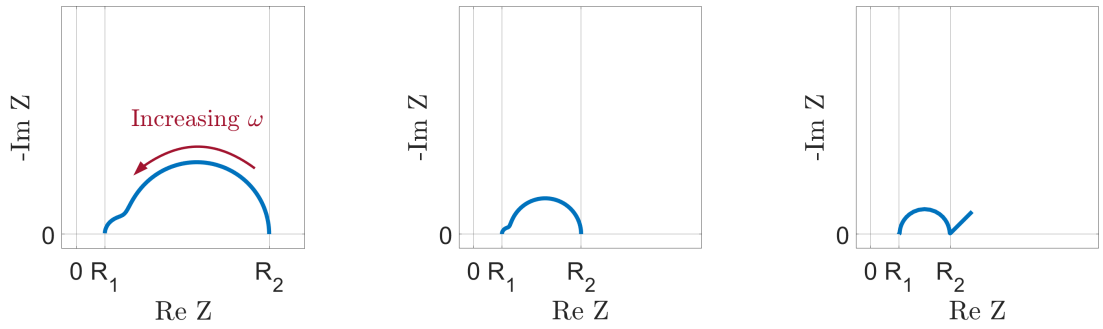

Figure 2.4: Characteristic Nyquist curve for **(a)** the activation region, **(b)** the ohmic region and **(c)** the mass transfer region. The frequency, ω, increases as indicated in **(a)**. Characteristically, there are two semicircles that decreases in size with higher current load. These can sometimes be indistinguishable [7]. R_1 and R_2 indicates the high and low frequency intercept respectively.

2.6.3 Electrical Elements

The behaviour seen at low frequencies in Figure 2.4**c** originates from the mass transport of oxygen to the TPB as it becomes limiting. This could not be modelled with the components in section 2.6.1, instead a Warburg element is included. The Warburg element impedance is defined as

$$Z = \frac{A_W}{\sqrt{\omega}}(1 - i), \tag{2.18}$$

where A_W is the cathode Warburg coefficient. This is called an infinite Warburg and gives a line with a 45° incline in a Nyquist curve. It corresponds to an infinite diffusion layer [20, 25]. In real cases, the low frequencies curve down to the real axis again since the fuel cell diffusion layer is not infinite.

The EDL is not a perfect capacitor. Instead, the semicircle seen in Figure 2.3**b** is often depressed for a real fuel cell. For a more realistic behaviour, the capacitor can be replaced by a constant phase element (CPE) [11]

$$Z(\omega) = \frac{1}{Q\omega^n e^{in\pi/2}}. \tag{2.19}$$

The parameter Q depends on the choice of n, which has a range between -1 and 1. The CPE does not correspond to one single electrical component; with a change of n, the behaviour of the component changes. For $n = 1$, the CPE is a capacitor (with a capacitance Q), while for $n = -1$, it is an inductor ($Q = 1/L$). $n = 0$ results in the impedance of a resistor ($Q = 1/R$), and $n = 1/2$ achieves the impedance of an infinite Warburg component [11]. Other choices of n thus describe a mix of behaviours and bring more freedom to modify the equivalent circuit to match impedance data. The CPE can therefore not be connected to any specific physical transfer rate until a choice of n is made. Choosing a value of n near 1 therefore describes a non-ideal

capacitor, which could be interpreted as an EDL [11].

2.6.4 Data Fitting

As described above, one effective approach to analyse the EIS response has been to use equivalent circuit models. In order to evaluate a chosen equivalent circuit, the circuit first needs to be fitted to the EIS data. Two major strategies used to fit the data are:

- analytical approach (also called the graphical method)
- numerical curve fitting

The analytical approach is straightforward: tune the parameters manually to best fit the data. The numerical curve fitting is more popular since it is fast and easy to use. It is commonly implemented with a non-linear least square method, which finds a local minimum, hence it is dependent on the starting guess [11].

3

Case Setup

The supplied experimental data were based on single fuel cell experiments with a geometric area of 5 cm^2. Two different fuel cells were experimented on: a fuel cell with a Nafion 212 membrane (fuel cell A) and a Gore-Select membrane with unknown parameters (fuel cell B). The Gore membrane has similar properties to Nafion, in that they are made of the same kind of polymer (perfluorinated sulphonic acid based polymers), but is also reinforced in order to increase the durability [31]. Overall, it has a lower conductivity compared to Nafion membranes [32]. All other components, (electrodes, flow field channels) had the same parameters. However, these parameters may have slight differences due to small variations in the production. See Appendix A for all physically relevant parameters of the fuel cell.

3.1 Lab Setup

The fuel cells were fed with an Argon-oxygen gas mix on the cathode side corresponding to the nitrogen/oxygen ratio in air with a volumetric flow rate of 400 mL/min. On the anode side, pure hydrogen gas (99.995%) was fed at 140 mL/min. The lowest stoichiometric ratio was calculated[1] to be ∼1.7 for the HOR and ∼2.2 for the ORR at the highest current density (approximately 1 A cm^{-2}). Inlet flows were at atmospheric pressure and were pre-heated as well as humidified to match the chosen conditions. The fuel cell operation conditions are listed in Table 3.1, where the humidity is specified by the RH. All experimental data was performed with no back pressure.

Table 3.1: Inlet flows state description for each experiment. *A* denotes the PEM fuel cell with a Nafion membrane, *B* denotes the fuel cell with a Gore membrane.

States	T [°C]	RH [%]
A	80	100
B.1	80	100
B.2	40	100
B.3	40	41

[1]The calculation is presented in Appendix B.

3.2 Physical Model

The GT fuel cell model was set with the same parameters as each experiment, which are also listed in Appendix A. It was further calibrated by matching relevant polarisation curves in Table 3.1. To calibrate the GT model, the OCV was tuned by setting a constant OCV voltage loss so that near zero current resulted in the same output voltage as the corresponding experiment. Next, GT Suite's optimizer was implemented to minimise the following residual based on the polarisation curve

$$r_{opt}(V_{model}) = \sum_{i=1}^{p} \frac{|V_{DC,i} - V_{model,i}|}{V_{DC,i}}, \tag{3.1}$$

where p is the number of points over the polarisation curve to fit the model to. The measurements i were chosen to be evenly distributed in order to capture each region of the polarisation curve. $V_{model,i}$ is the voltage output from the GT model, while $V_{DC,i}$ was the direct current output from the experimental cell. While the lab was performed using a potentiostat, the model was fed with a DC current instead (corresponding to a galvanostat). The chosen calibration parameters were the charge transfer coefficient α in (2.7) to manipulate the activation region, the membrane conductivity factor σ_{11} in (2.11) for the ohmic region, and the porosity ε of the electrodes for the mass transport region. The optimizer used a genetic algorithm with 10 individuals (sets of chosen α, σ_{11} and ε) and was executed for 20-50 generations for both fuel cells (i.e. 200-500 individuals). The individual with the lowest residual was chosen and its parameter values were implemented. After the fuel cell models were calibrated from polarisation curves, their prediction for polarisation curves at other temperatures and humidities were qualitatively compared to expected behaviour from literature.

The GT model consisted of a fuel cell component as well as a current source, as previously mentioned. In order to achieve the correct operational states, two inlet and outlet components were incorporated, one for the anode and one for the cathode. These supplied the reactants and transported away the products and excess. In the inlet and outlet components, many of the boundary conditions from the experiments were set such as temperature and pressure. In order to get a stable model, a humidifier was used to calculate the amount of water that should be supplied at the given state instead of setting a value from the experiments. This lead to a more robust model for variations from the initial state. Note also that the model needed a nitrogen mixture in order to function, while the experiments were operated with an argon-oxygen mix. This lead to that the cathodic inlet was modelled to have an air mixture, which modified the diffusion coefficients of the gas mass transport.

3.3 Equivalent Circuit

Two equivalent circuit models were chosen, namely the Randles circuit and the flexible EC (fEC) model, which are presented in Figures 3.1. These models were selected as starting points for the equivalent circuit model. The components of the

model were fitted to the EIS data using a complex non-linear least squares method. In Python, the SciPy function *least_squares* was used to minimise the residual vector, which was defined as

$$r(Z_{EIS}) = \frac{|\ \mathrm{Re}\,(Z_{EIS}) - \ \mathrm{Re}\,(Z_{EC})\ | + |\ \mathrm{Im}\,(Z_{EIS}) - \ \mathrm{Im}\,(Z_{EC})\ |}{|Z_{EC}|}, \tag{3.2}$$

where Z_{EIS} and Z_{EC} is the impedance of the experimental data and the calculated response from the EC model respectively. This fitting was performed on all the negative imaginary impedance points only.

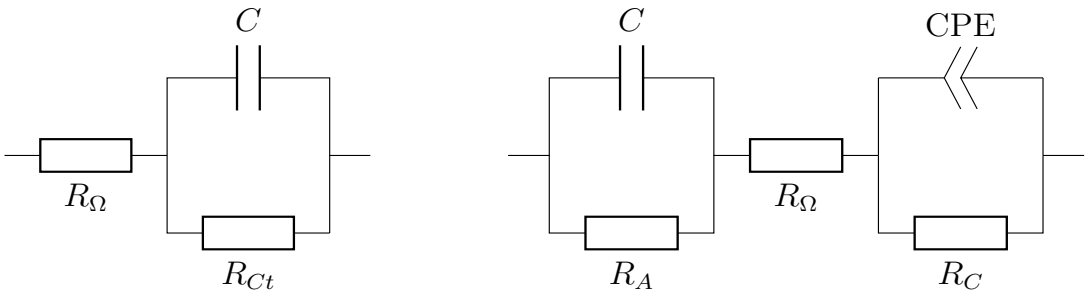

Figure 3.1: The chosen equivalent circuit models: (left) the Randles circuit and (right) the flexible equivalent circuit (fEC).

4
Results and Discussion

In this section, the results are presented and discussed for the EC model and GT-SUITE model. The GT model is evaluated for how well it performs compared to the experimental data. Connections between the EC model and GT model are investigated.

4.1 Experimental Data

The overall experimental process in time is shown in Figure 4.1 for experiment A. The cell was exposed to a steady voltage using a *Gamry* potentiostat. After 30 seconds at a certain voltage, a superimposed AC voltage was introduced with a 4 mV amplitude and frequency of 2 Hz - 100 kHz. The DC voltage step and AC voltage sweep is referred to as a cycle. Some current density cycles are more stable than others. More stable cycles are indicated with a red ring. Some of these rings might be a little unstable, but the aim is to capture the behaviour over the whole experiment and therefore a distribution of points that covers the whole current spectrum is needed. Note that higher currents are less stable. The experiments were operated with a constant volumetric flow rate, which with increasing current also decreases the stoichiometry reactant, which has been found to increase the time to reach steady state [33]. In Appendix C, fuel cell B is presented and show similar behaviour as in Figure 4.1.

At 0.7 V, 0.63 V, 0.55 V and 0.45 V, sudden drops in current can be seen in Figure 4.1. A hypothesis as to why they occurred is that water droplets were formed at these times in the gas diffusion layer or catalyst layer. These droplets block gas reactants from the TPB. As the droplets are removed, the fuel cell recovers. An article by Hartnig et al. somewhat support this hypothesis, as they found that small cyclic water eruptions occurred in the gas diffusion layer during their operation of a PEM fuel cell [34].

Polarisation curves were generated by taking the last data point of the measured current density for each fixed voltage (the last black point at each current density). These curves are shown in Figure 4.2 for experiment A and B. The voltage ranged between 1 to 0.4 V. It was not further decreased in order to avoid degradation caused by starvation. Therefore, there is no clear indication of a mass transport region. In total, 17 EIS were performed across the polarisation curve.

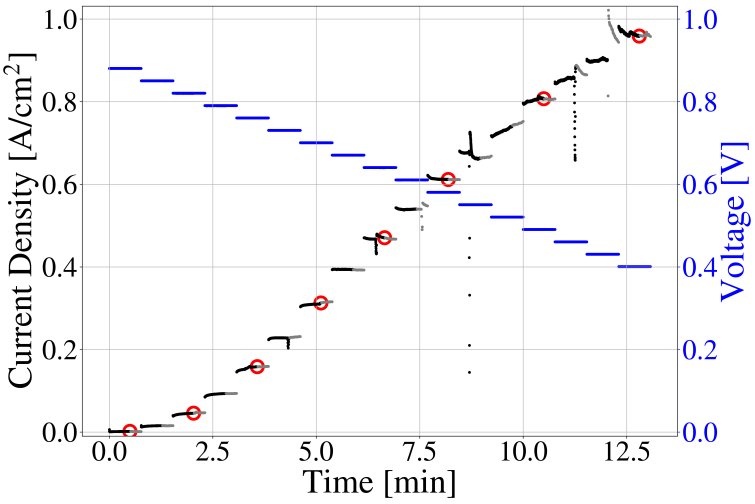

Figure 4.1: The transient data of the current response from the potentiostat (shown in black), including the impedance spectroscopy at the end of each voltage step (shown in grey). Red circle markers show which voltage steps that where chosen to calibrate the polarisation curve for the GT model based on experiment A, 80 °C, 100 % RH. The blue lines indicate the drawn voltage from the cell at each time.

For fuel cell B, something happened in between the experiments. Note that for a relative humidity of 100% the lower temperature of 40 °C has a higher voltage at any given current density compared to the higher temperature of 80 °C, as can be seen in Figure 4.2. This is the opposite of what is expected from literature and it is probably caused by degradation, which altered the physical fuel cell parameters. Comparing these experiments is similar to comparing different fuel cells.[1] Therefore, the experiments from fuel cell B should be usable on their own, but cannot be compared with each other.

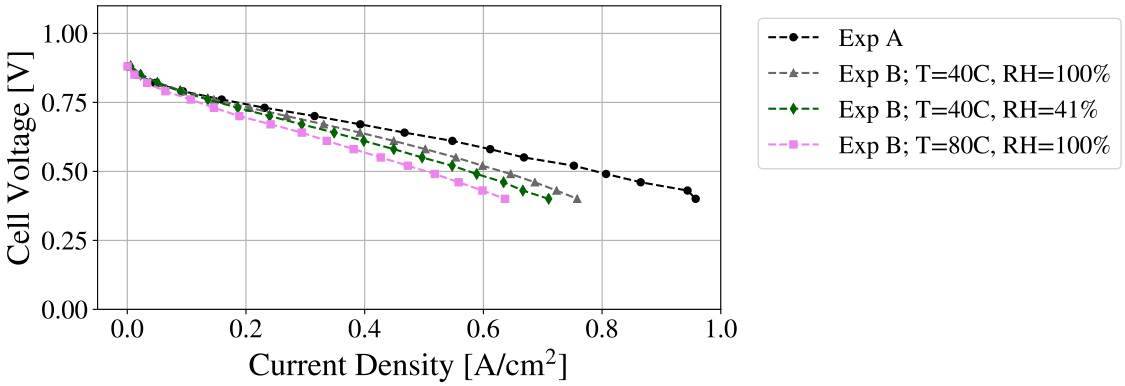

Figure 4.2: Polarisation curves of the experimental data.

[1]The cause is outside the scope of this project, but a hypothesis is that the cell was operated with an initially dry membrane during some of the experiments.

4.2 GT - SUITE Model

The GT model was calibrated according to each set of operating conditions as described in Table 3.1. The resulting values of all calibration parameters are listed in Appendix A. The calibration for experiment A is shown in Figure 4.3. Values circled in red are calibration points for the algorithm. When the genetic algorithm was allowed to vary the porosity, it reached the unlikely value of 0.97 (porosities of gas diffusion electrodes are generally in the range of 0.7-0.8 [35]). The result of that calibration can be seen in Figure 4.3**a**. In Figure 4.3**b**, the same calibration procedure, but with fixed porosity of 0.7, is shown with no visible difference. Therefore, the GDL porosity has a negligible effect on the polarisation curve. This is due to the voltage range not reaching the concentration region. A similar result was given for fuel cell B as shown in Appendix D, thus the porosity is hereafter fixed to 0.7.

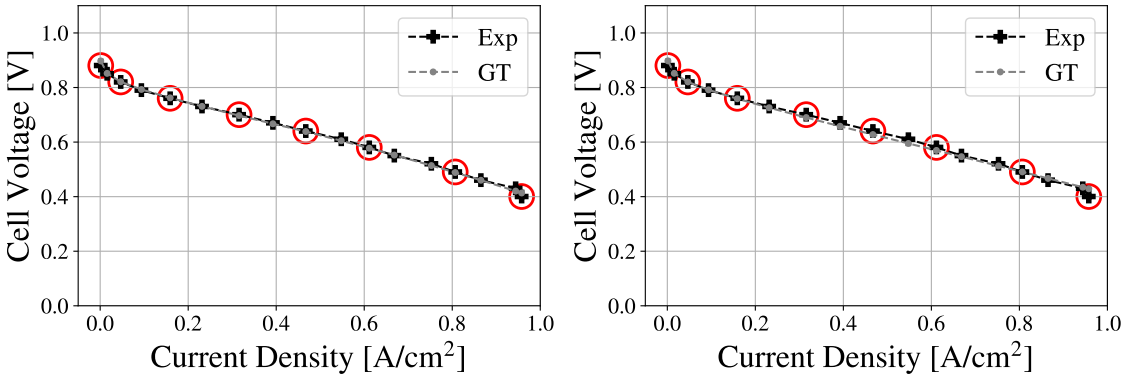

(a) **(b)**

Figure 4.3: Calibration of experiment A at 80 °C, 100% RH at both inlets (anode and cathode). Black line indicates the experimental data and grey line show the result from the GT model. Red circles mark the points that the model used to calibrate the model. In **(a)** the porosity set during calibration by the genetic algorithm was 0.97 and in **(b)** the porosity was fixed to 0.7.

Similarly, the calibration process was repeated for fuel cell B with the resulting polarisation curves as shown in Figure 4.4**a** and 4.4**b**. These single state calibrations show good alignment to the experimental data. Note that the calibration of the 40 °C, 41% RH state is not included. Lower humidity fuel cell calibrations were not successful due to difficulties in simulating a Gore membrane using a Nafion based model, but also because the membrane humidity is overall unknown. Letting the membrane humidity approach the same humidity as the inlet gases result in incompatible polarisation curves to the experimental data, hence the approach used so far would have to be drastically changed. Only two parameters were calibrated using a genetic algorithm (σ_{11} and α) and there are more parameters that can be adjusted for a more suitable fit, e.g. water transport rate factors in the membrane. However, these factors are unknown and outside the scope of this thesis.

It is possible that the membrane humidity for each experiment did not reach steady

state. For a fuel cell with initially low humidity, the membrane is able to absorb any produced water at the cathode, thus the membrane humidity increases for each voltage step. Assuming that the membrane could not measurably exceed 100% RH, the membrane humidity would then barely vary if the membrane humidity started at 100% and therefore reach steady state quicker. The membrane humidity response would then be slowest for experiment B.3 (40°C, 41% RH). Andrea Ramírez-Cruzado et. al (2020) found hysteresis effects in forward and backward current density stepping using similar time steps; they believe it was caused by differing membrane water content [36]. Therefore, the DC time duration for each voltage step in experiment B.3 could be too short to stabilise the humidity. Jay Benziger et. al (2005) also found that the relative humidity was not steady until 10 000 seconds had passed and they suggested it was caused by a mechanical swelling processes of the membrane, which was restricted by the surrounding components [37]. The membrane restriction is in this case unknown, but could also have affected the humidity response time.

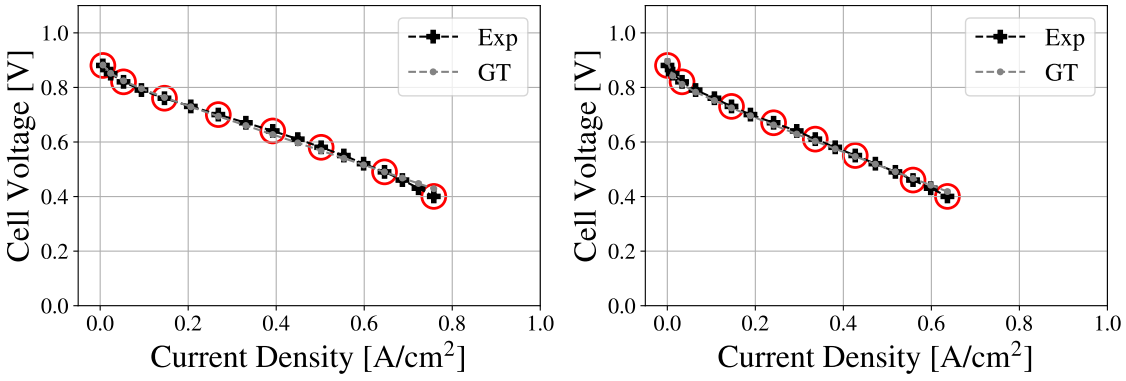

(a) **(b)**

Figure 4.4: Calibration of fuel cell B at the two different temperatures **(a)** 80 °C and **(b)** 40 °C. Both at 100% RH. Black line indicates the experimental data and the grey lines show the result from the GT model. Red circles mark the points that the model used to calibrate the model.

4.2.1 GT Extrapolations

A small investigation was performed to see if the GT model behaved as the literature predicts. This was done by changing the operational temperature from each single state calibration model, while keeping the other parameters fixed. The 40 °C calibrated model was simulated at 80 °C and its resulting polarisation curves are shown in Figure 4.5**a**. An increased performance is seen at higher currents as expected, and the activation is lower than the 40°C case. The literature predicts that the OCV decreases with higher temperature due to higher membrane permeability, thus increasing the hydrogen crossover rate [38]. The OCV was affected as predicted despite being set as constant in GT (which is further described in Section 4.2.3). That is because the GT model does not account for hydrogen crossover

losses explicitly in the OCV voltage loss, but is instead included in the activation loss from its reactant concentration dependency. The behaviour of the polarisation curves in Figure 4.5**b** is similar: when the 80 °C model is operated at 40 °C, the same behaviour is seen but with a steeper ohmic region for both curves, which was possibly caused by degradation.

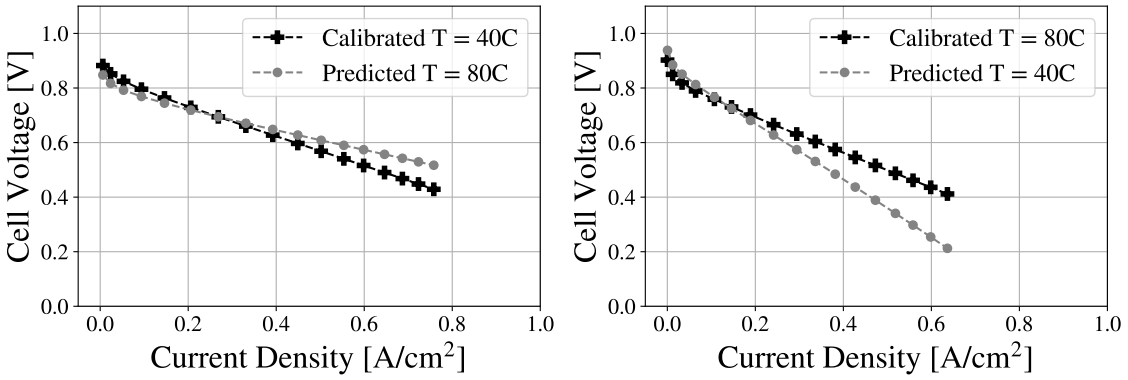

(a) **(b)**

Figure 4.5: Polarisation curve prediction at a different temperature. In **(a)** the calibrated GT model for experiment B.2 at 40 °C and 100% RH presented in Figure 4.4**b** is used to predict a temperature of 80 °C. In **(b)** the calibrated GT model for experiment B.1 at 80 °C and 100% RH presented in Figure 4.4**a**, is used to predict a temperature of 80 °C. The only parameter changed in the prediction is the temperature.

4.2.2 Combining Calibrations

To investigate the possibility to include multiple operating conditions in the GT fuel cell model, polarisation curves for both 40 °C and 80 °C at 100% RH were calibrated against simultaneously, keeping in mind that they are not compatible due to degradation. The resulting polarisation curve at each temperature is compared with experimental data in Figures 4.6**a** and 4.6**b** for temperature 40 °C and 80 °C respectively. Four points from each experiment (polarisation curve) were used as calibration points marked with red circles. As shown in both figures, the simulated polarisation curves have decreased in accuracy as both states were included. It is to be expected considering the degradation between the cases.

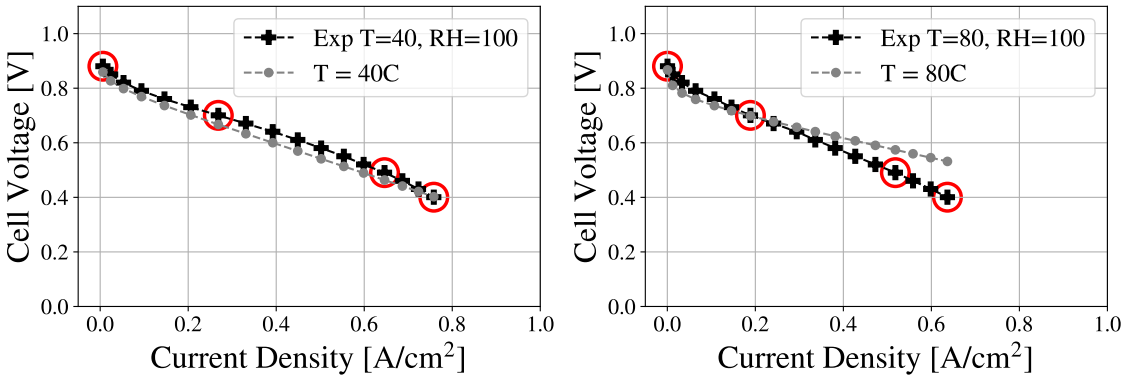

(a) **(b)**

Figure 4.6: Calculated polarisation curves using calibrated GT models from two states of fuel cell B (80 °C and 40 °C at 100 % RH in black). Red rings marks the points used in the calibration. In **(a)** the experiment B.2 at 40 °C and 100% RH is shown, together with the calculated polarisation curve at 40 °C (grey). **(b)** is the same, but for 80 °C.

4.2.3 Voltage Losses

The GT model allows for an estimated breakdown of each voltage loss contribution, categorised as activation, ohmic and concentration losses. By comparing the voltage losses, a discussion can be made regarding if the polarisation curve calibration has accurately captured the behaviour of each voltage loss. Note that the voltage losses in GT are calculated on the assumption that the OCV is

$$OCV = E^0 - k_{OCV} \tag{4.1}$$

where the constant k_{OCV} is fitted such that the lowest current datapoint aligns with the output at the same current. They are listed for each calibration in Appendix A.

In Figures 4.7 a-c, the voltage losses are shown for experiment A, with porosity 0.97. As expected, the activation loss increased the most at low current, the ohmic loss increased linearly from zero and the concentration loss barely impacted the fuel cell but does increase for higher current. Similar behaviour can be seen in all voltage loss curves for fuel cell B as well, which are presented later. Note, the ohmic losses are quite high and are further discussed later in comparison to the ohmic resistance from the equivalent circuits, which are then shown to be much lower.

The voltage losses for the same operational conditions but with the fixed porosity of 0.7 are shown in Figures 4.8 a-c. By comparing the concentration loss in Figures 4.7**c** and 4.8**c**, the low porosity resulted in a slightly higher concentration loss. Since they both are calibrated to fit the polarisation curve (which is essentially the combined contribution of all voltage losses) they are both well calibrated to the experimental polarisation curve. This results in that the ohmic and activation loss compensate for the decrease in concentration loss. As seen in Figure 4.8**b** the ohmic loss has

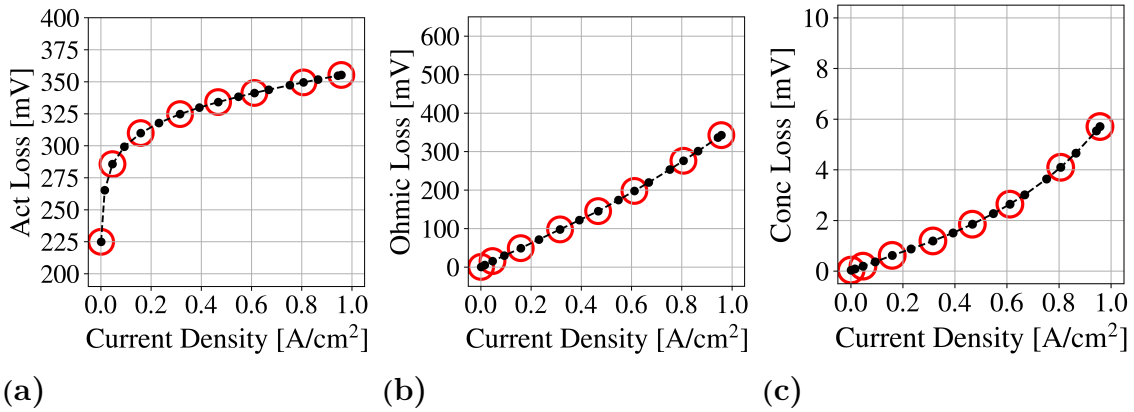

(a) **(b)** **(c)**

Figure 4.7: Modelled voltage losses of experiment A in GT at 80 °C, 100% RH with porosity 0.97.

decreased compared to in Figure 4.7**b**, where the porosity was 0.97. The activation loss stayed roughly the same as seen in Figures 4.7**a** and 4.8**a**. The porosity of 0.7 can then be assumed with little consequence, as both cases result in a negligible difference in distribution of voltage losses.

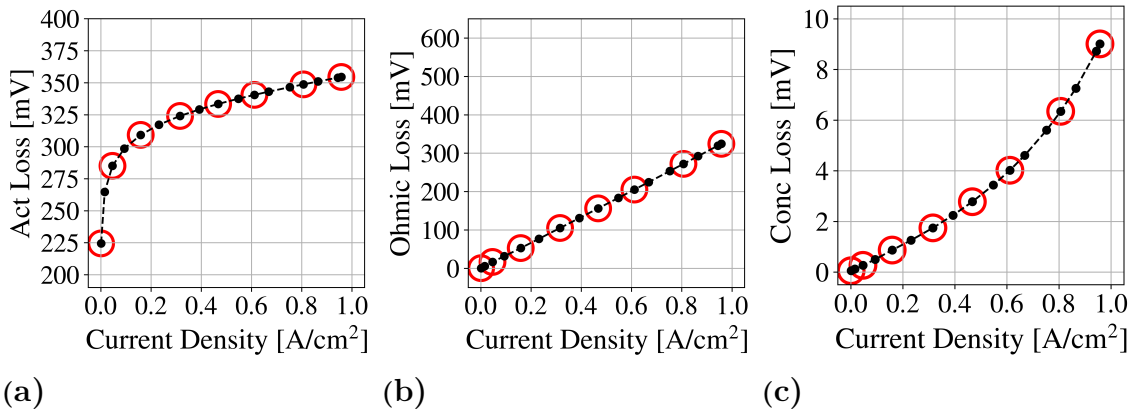

(a) **(b)** **(c)**

Figure 4.8: Modelled voltage losses for experiment A in GT at 80 °C, 100% RH with fixed porosity 0.7.

Next, in Figures 4.9 a-c the voltage losses for experiment B.1 at 80 °C and 100% RH is shown. Similarly to experiment A, the porosity had the same lack of effect on the polarisation curve and was therefore set to 0.7 for all experiment B states (the comparison is shown in Appendix D). In comparison to the activation loss of experiment A in Figure 4.8**a**, it is overall lower but close. The ohmic loss in Figure 4.9**b** is much higher, which may experimentally be due to the change from a Nafion membrane to a Gore membrane, but also partly the aforementioned degradation of the cell. The concentration loss in Figure 4.9**c** reached a lower value due to the low current density.

The voltage losses for experiment B.2 at 40 °C and 100% RH are shown in Figures

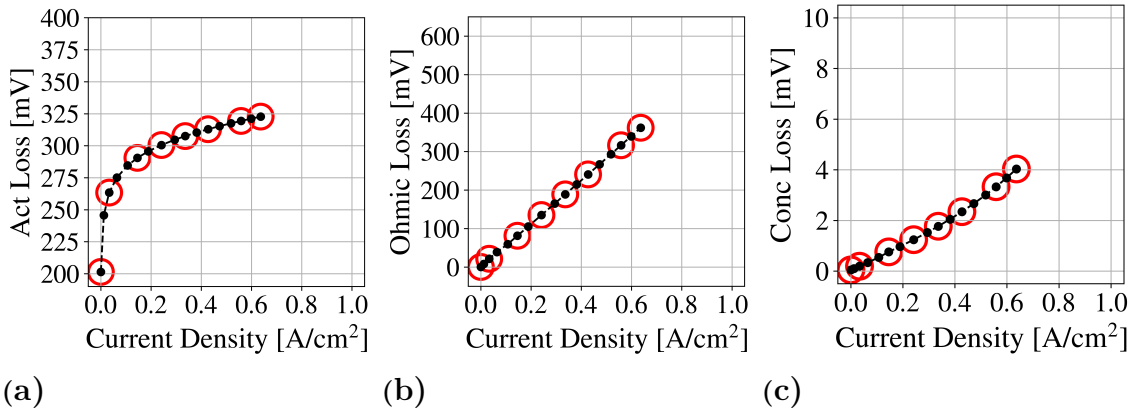

(a) **(b)** **(c)**

Figure 4.9: Modelled voltage losses for experiment B.1 in GT at 80 °C, 100 RH with fixed porosity 0.7.

4.10 a-c. In comparison to experiment B.1 at 80 °C and 100% RH, the activation losses are overall slightly higher. This corresponds well to literature, in that the activation loss is higher for lower temperatures. The ohmic loss is lower, but not by much. The concentration loss decreased for the lower temperature when comparing Figure 4.10**c** with Figure 4.9**c**.

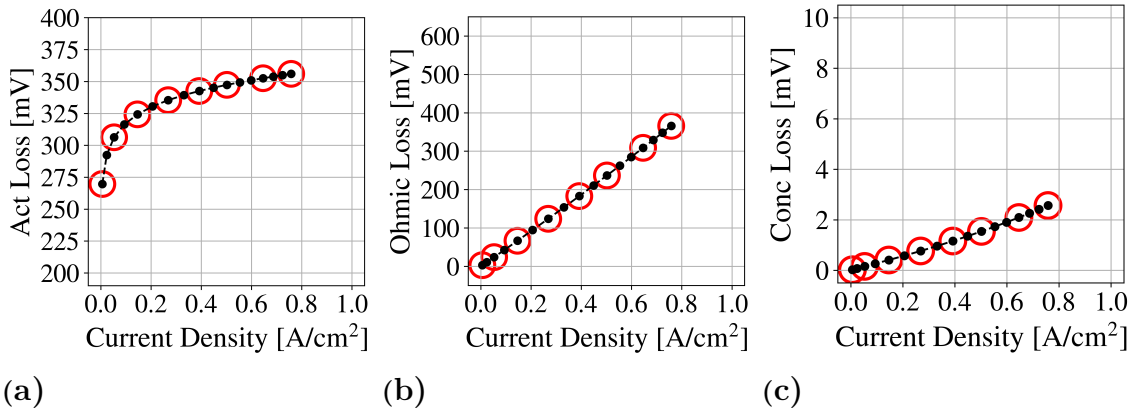

(a) **(b)** **(c)**

Figure 4.10: Modelled voltage losses for experiment B.2 in GT at 40 °C, 100% RH.

The extrapolation of the models to other temperatures show changes in the voltage losses as well. In Figures 4.11 a-c, the voltage losses for fuel cell B, calibrated according to data-set 40 °C, 100% RH, and then changed to a temperature of 80 °C are shown. Figure 4.11**a** shows an initial activation loss that is lower for 40 °C, 100% RH in Figure 4.10**a**. This is what is expected from literature; an increase in temperature leads to a increase in exchange current density (j_0 in (2.3)) resulting in a decrease in activation overpotential [39]. The decrease of activation loss may be understated due to the inclusion of hydrogen crossover (as described earlier).

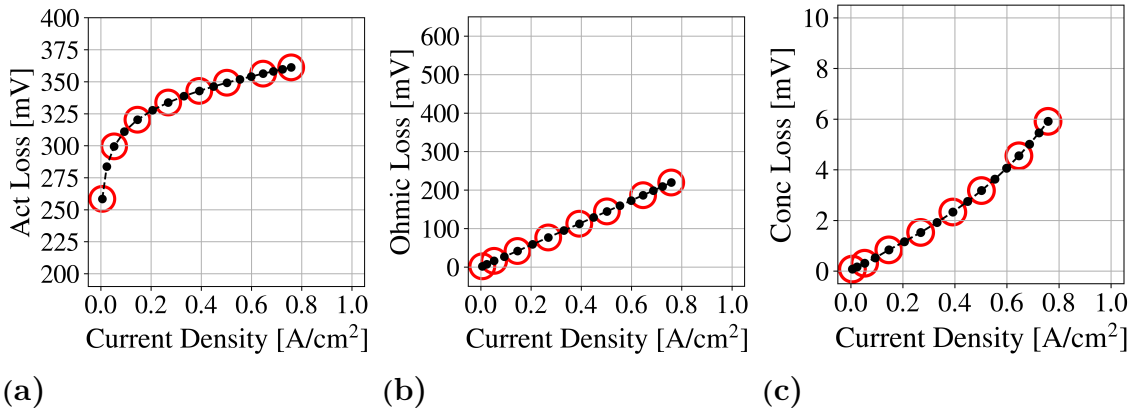

Figure 4.11: Modelled voltage losses of fuel cell B in GT using a model calibrated for 40 °C, 100 RH, and then extrapolated to 80 °C, 100 RH.

Additionally, it can be seen that the ohmic voltage loss is halved when comparing the 40°C calibration in Figure 4.10**b** with its extrapolation to 80°C in Figure 4.11**b**. The conductivity of the membrane is both temperature and water content dependent, and in both temperature cases, the humidity was set as the same. However, a 100% RH corresponds to different amounts of water at different temperatures. 100% RH in 40 °C and 80 °C at the inlet correspond to different amounts of incoming vapour, 0.07 and 0.44 gas molar fraction on the cathode side respectively. In reality, the two inlet gases might hydrate the membrane to different extents. Therefore, the membrane would not necessarily behave the same way for both inlet gases and the membrane humidity may differ from the humidity of the surrounding gases in the electrodes during the experiment. Note that the membrane conductivity model is also built on the assumption of a Nafion type membrane. In total, since the membrane humidity is unknown and the model assumes a Nafion type membrane, the GT fuel cell B model's ohmic loss could be less accurate. As the original experiment B.2 model at 40 °C is calibrated with a possibly less-suited membrane conductivity model against a polarisation curve, the sum of all other voltage losses are impacted with a corresponding error to match the polarisation curve.

When the 80 °C, 100% RH model is extrapolated to 40 °C, 100% RH, the resulting voltage losses are as shown in Figures 4.12 a-c. The activation losses barely increased at the lowest current density but is otherwise the same as for the higher temperature of 80°C in Figure 4.9**a**. The ohmic losses in Figure 4.12**b** have increased as expected from literature, with an endpoint of almost 600 mV in comparison to 350 mV in Figure 4.9**b**. Figure 4.12**c** shows a decline in concentration losses at the lower 40 °C temperature in comparison to Figure 4.9**c**. The modified concentration loss at 40°C could be caused by the lower vapour molar fraction since the molar reactant fraction is then higher. The activation loss was also expected to be overall higher for a 40 °C, 100% RH case, but may be underestimated and partly attributed to the ohmic loss instead.

Overall, these GT simulations require a careful choice of membrane humidity model

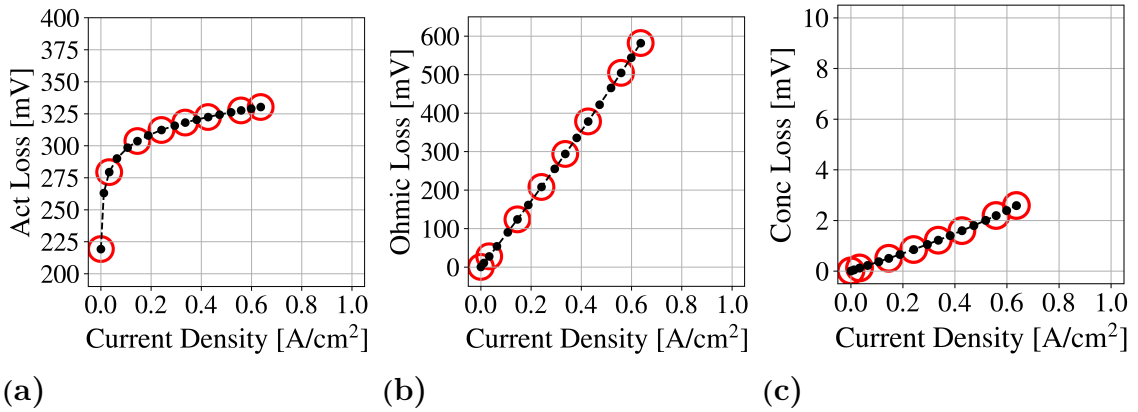

(a) (b) (c)

Figure 4.12: Modelled voltage losses of fuel cell B in GT using a model calibrated for 80 °C, 100% RH, and then extrapolated to 40 °C, 100 RH.

to match the membrane type, as well as more experimental data to further increase the accuracy of extrapolations of operating conditions.

4.3 Equivalent Circuits

The EIS response from experiment A is presented in Figure 4.13 for the lowest and highest current as well as an intermediate current. Recall that only the negative imaginary impedance is of interest, since the high frequency inductance as of yet is thought to be mainly related to things outside the fuel cell. The red dots in the figure is the fitted EC model, in this case the Randles circuit. Each point correspond to the same frequency point as the experimental data as indicated in the figure. The negative imaginary impedance for experiment A spans from 969 Hz to 2 Hz. The Randles circuit follows the pattern of the experimental data. It is a fitting model when the experimental data is close to a displaced perfect semicircle, which is seen at intermediate currents. It follows the overall pattern of the experimental data for all currents, but is unable to capture deviations from a semicircle.

The response from the fitted fEC model as was introduced in Figure 3.1 is presented in Figure 4.14. Similar to Figure 4.13, where the response from the Randles circuit was presented, the fEC model is fitted against experiment A and used the same frequency region and current densities. For low currents, the fitted curve follows the high frequency behaviour as expected. As suggested before, the anodic part is negligible, but as seen here it helps the fitting. Therefore, the fEC model achieved a closer fit of the high frequency intercept without sacrificing the fitting of the larger semicircle. At intermediate currents, the curve is more depressed than a perfect semicircle, which the non ideal capacitor (the constant phase element) helps with.

The fEC model is an overall better fit. This can also be seen for the residuals shown in Figure 4.15, where the fEC model has an overall lower residual. As expected, more flexibility lead to a better fit. A less flexible model cannot follow every devi-

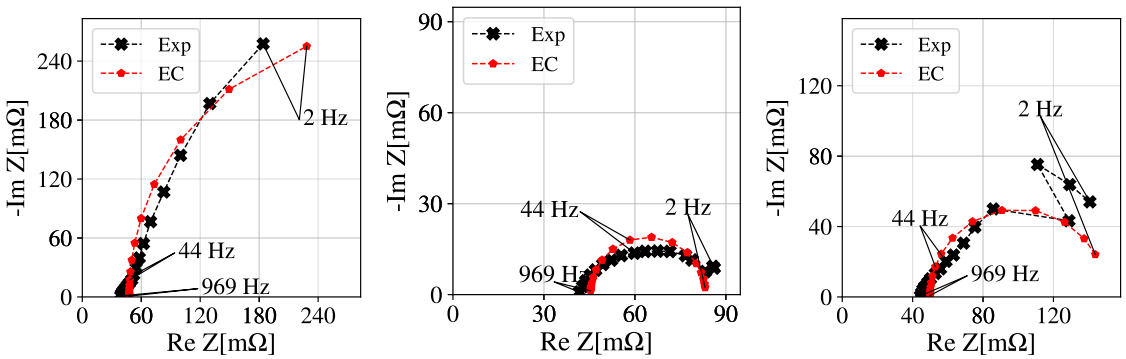

(a) 1.2 mA/cm^2 **(b)** 480 mA/cm^2 **(c)** 960 mA/cm^2

Figure 4.13: Nyquist curves for the Randles circuit and the experimental (EIS) data A. The EC model is fitted with non-linear least squares and the frequency spans between 2Hz to ∼1kHz as indicated.

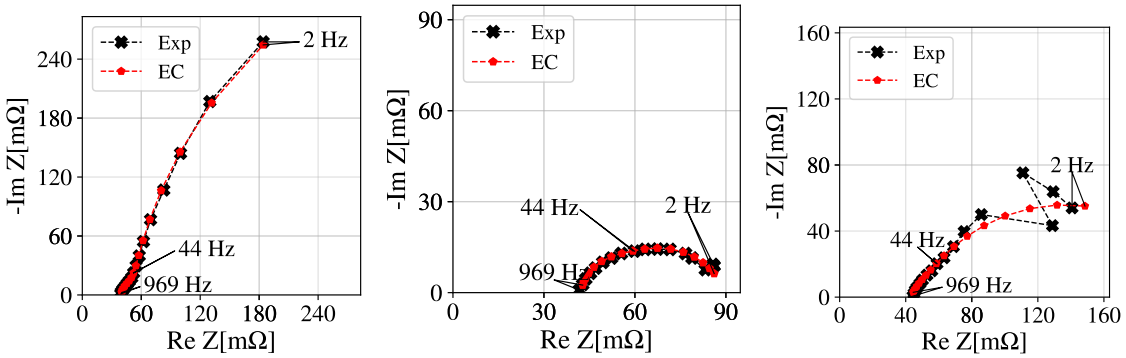

(a) 1.2 mA/cm^2 **(b)** 480 mA/cm^2 **(c)** 960 mA/cm^2

Figure 4.14: Nyquist curves for the experimental (EIS) data A as black crosses and the fEC model as red dots. The EC model is fitted with non-linear least squares and the frequency spans between 2Hz to ∼1kHz.

ation, while a more flexible model has the risk to fit the noise of the data, called overfitting. The electrical components of the fEC model used here has a physical connection from the literature, which decreased the risk of fitting the noise.

As previously noted, the Randles circuit performs best at the intermediate current. This can also be seen in Figure 4.15**a**. This is where the experimental data is most similar to a displaced semicircle, which is what the Randles circuit assumes. This is expected in the ohmic region. Recall that the higher current was still in the ohmic region or transitioning to the concentration region as discussed in section 4.2, but is more noisy as seen in Figure 4.13**c**. For the fEC model, the residual is overall lower as seen in Figure 4.15**b**. This is expected from the comparison between the Nyquist curves fitting seen in Figures 4.13 and 4.14. As previously described, the improvement is due to the incorporation of the second parallel circuit and the con-

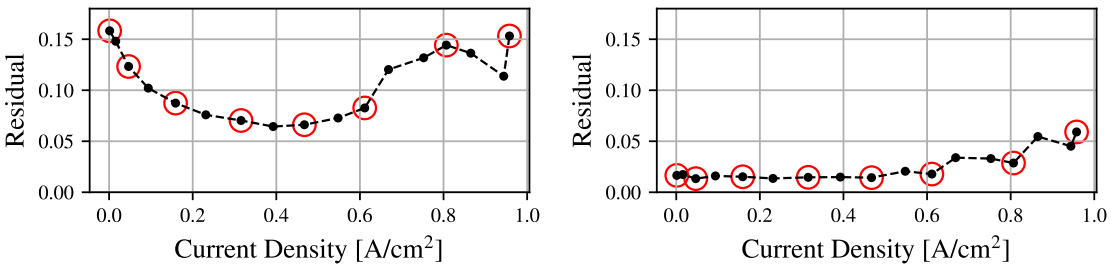

(a) **(b)**

Figure 4.15: Residual from EC models, where **a** is for the Randles circuit and **b** is for the fEC model, fitted against experiment A. The red rings indicate the stable current points chosen in Figure 4.1.

stant phase element. At low currents, the fEC model lowers the residual to the residual of the intermediate part. The model performs well in both the low and intermediate current regions.

The residual indicates that the fEC model performs worse for higher currents as seen Figure 4.15**b**. A fit can be poor due to several reasons. One possibility is that a chosen EC model is a poor representation of the general electrochemical processes occurring in the fuel cell. Another reason could be that the model is chosen to represent a specific current region and neglect components related to other current regions. This would lead to higher residual for those regions. This could be the case, but the most probable explanation for this ill fit is the data noise that can be seen in Figures 4.13**c** and 4.14**c**.

4.3.1 Electrical Components

The electrical components for the Randles circuit model is presented in Figure 4.16. As expected, the ohmic resistance shown in Figure 4.16**a** is close to constant. The variations is as previously mentioned probably caused by variations in the membrane humidity throughout the experiment and of course by noise.

The capacitance decreased with increased current to then return to the same value, as can be seen in Figure 4.16**b**. The capacitance of the Randles circuit model represent the EDL of the fuel cell, which absorbs charges to surfaces. The decrease with higher current could be a result of the higher water production, which leads to higher membrane conductivity. This leads to faster ion transfer though the fuel cell and therefore lower static charge build up to form the EDL. At around 0.7 A/cm^2, the capacitance returns to the original value and stays constant for higher currents. This may be caused by excessive water production hindering the gaseous transport that can increase the EDL effect again.

The charge transfer resistance R_{Ct} defines the size of the semicircle, which can be seen to decrease in size to then increase again in Figure 4.16**c**. The decrease is ex-

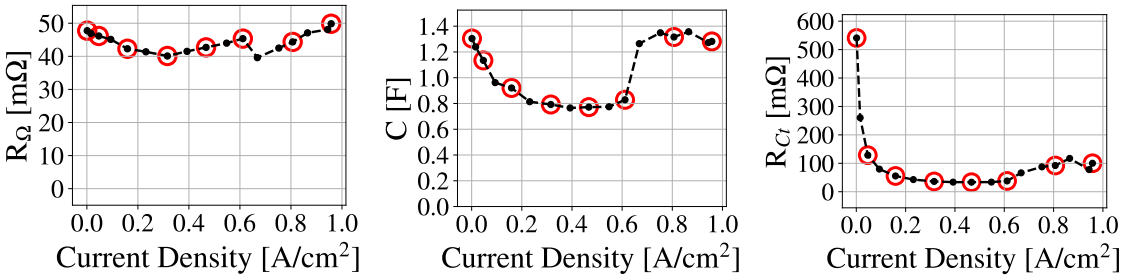

(a) **(b)** **(c)**

Figure 4.16: The electrical components in the fitted Randles circuit model for experiment A. **(a)** is the ohmic resistance, **(b)** the capacitance and **(c)** the charge transfer resistance.

pected as mentioned in section 2.6.2. The increase at high currents could be caused by the noise in the data. It could also be that the experimental data tends to an infinite Warburg element, resulting in a larger semicircle, indicating mass transport resistance. The cell is likely affected by the high water production and resulting mass transport limitations after this current point. This indicates that the cell is transitioning into the concentration region.

The electrical components of the fitted fEC model is shown in Figure 4.17. The ohmic resistance resembles the same result as from the Randles circuit, although small differences exist. The differences are mainly at low currents, where the Randles circuit tries to compensate for not having a second parallel circuit. As a consequence, it underestimates the difference between the high and low frequency intercept as can be seen in the Nyquist curve in Figure 4.13. The cathodic resistance shown in Figure 4.17**d** correspond to the charge transfer resistance in the Randles circuit model and shows the difference between the high and low frequency more accurately.

The proposed anodic parallel circuit components in the fEC model are fairly constant at low current and then increase or decrease for the capacitance, C and anodic charge transfer resistance, R_A respectively. As the anodic part has such a small contribution to the overall impedance response, it is difficult to differentiate between it and the larger semicircle. Therefore, conclusions from the anodic part should be drawn carefully. In PEM fuel cell simulations, the main concern is the limiting cathodic behaviour. As the anodic contribution is small, there is a risk that the anodic components influences other processes when the anodic part is negligible. This could be the case for higher currents, where the previously small semicircle has disappeared. As seen in Figures 4.17**b** and 4.17**c** the components increase and decrease respectively. This could be an indication that the fitting of anodic parameters are not independent from those on the cathode side, but several elements affect the same frequency regions of the impedance curve. When R_A shrinks, it creates a small semicircle and with increased capacitance, the frequency points cluster at the high frequency intercept, creating an almost straight line, which can be seen in Figure 4.14**c**. To avoid the risk of anodic influence, a new model is introduced with

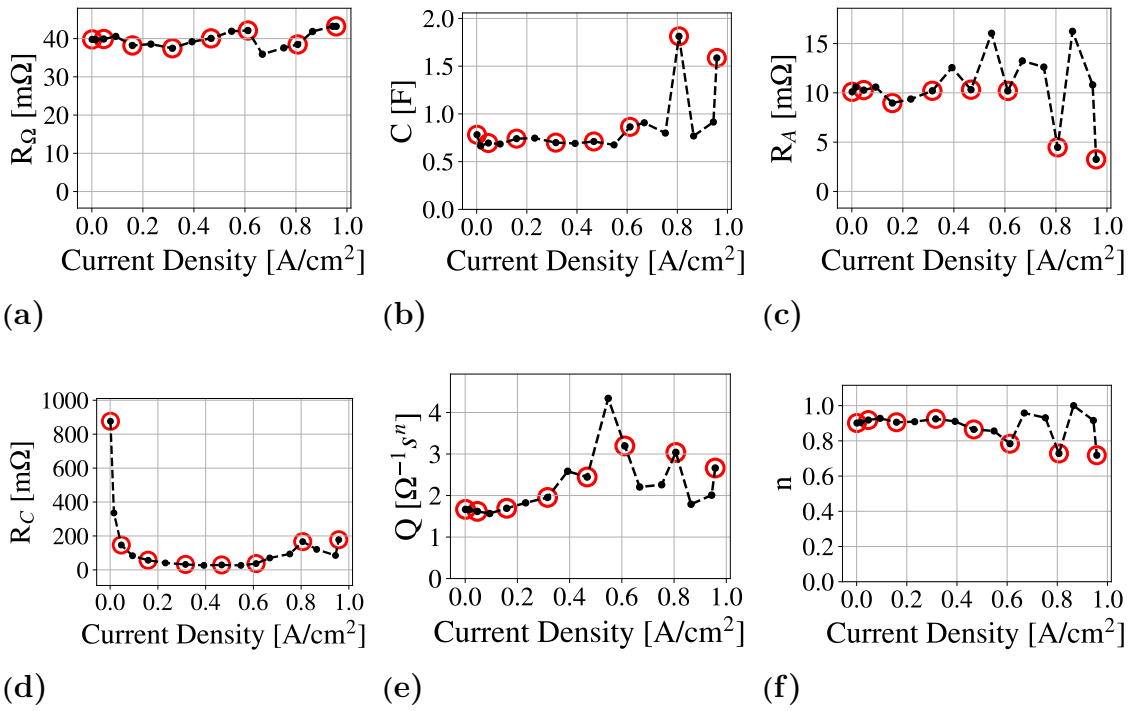

Figure 4.17: The electrical components in the fitted fEC model presented in Figure 3.1 for experiment A. **(a)** is the ohmic resistance, **(b)** and **(c)** is the capacitance and resistance respectively of the parallel circuit representing the anodic response. **(d)** is the resistance of the parallel circuit representing the cathodic response. **(e)** and **(f)** are the CPE components of the same parallel circuit.

a constant anode. The parameters were set to $C = 0.7$ F and $R_A = 0.1\Omega$ based on the fairly constant values at low currents. The anodic component is known to be negligible for all other currents and therefore set to constant values. This model is referred to as the flexible EC with constant anode (fcaEC) model.

As for the CPE's components in Figure 4.17, Q is around 2 $\Omega^{-1}s^{-n}$ until the current density reaches 0.4A/cm^2, where it varies between 2-4 $\Omega^{-1}s^{-n}$. n impacts Q by changing how the semicircle behaves; it can become a more or less depressed semicircle. If the stable red rings are studied, n is roughly constant at low currents and then decreases after 0.4 A/cm^2. This is at the same point as Q increases. Note that the decrease of n at higher currents could be a possible indication that the fuel cell is approaching the concentration region, by approaching a Warburg element (recall that $n = 1$ is a capacitor and $n = 0.5$ is an infinite Warburg). It is similar to what was seen for the Randles circuit model.

To study what happens if a fixed nonideal CPE is used, a new model is introduced with a constant value of n. n roughly varies around 0.9 at low currents, if more uncertain high currents points are excluded. This model also includes a constant anode with the same values of C and R_A as the fcaEC model. This model will be referred to as flexible EC with constant anode and n (fcanEC) model. Both of the

new models decrease the flexibility, which makes for easier fitting as the impact of the start guess is lowered.

4.3.2 New EC Models

The new EC models are expected to have a worse or equally good fit as the previous model, since a more flexible model can always recreate the best result from a stricter model with constant components. The residuals for the new models are presented in Figure 4.18 and have no noticeable difference from the residual presented for the fEC model in Figure 4.15**b**. The constant models perform slightly worse for higher currents. Recall that this corresponds to where the components of the fEC model (C,R_A and n) deviated from constant values as seen in Figures 4.17**b**, 4.17**c** and 4.17**f**.

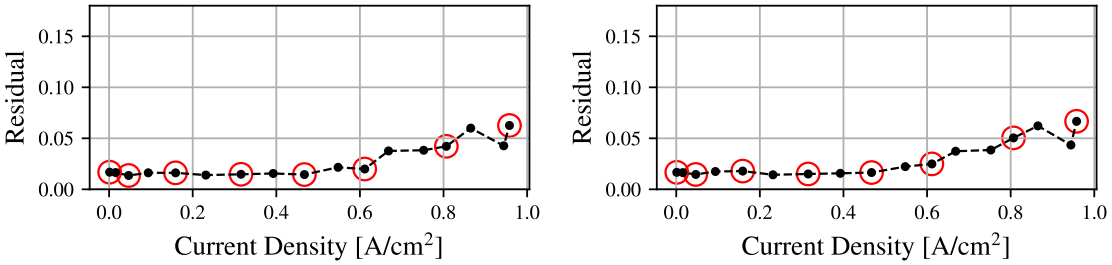

(a) **(b)**

Figure 4.18: Residual from the flexible EC models, where **(a)** is with constant anodic components and **(b)** is for constant anodic components and n, fitted against experiment A. The red rings indicate the stable current points chosen in Figure 4.1.

At first glance, the Nyquist curves look identical to the fEC model and are shown in Appendix E. The electrical components show what has changed more clearly, and are presented in Figure 4.19 and Figure 4.20. The ohmic resistances are as expected unchanged, since the model modifications should not affect that part. There seems to be small changes at higher currents for the cathodic resistance, R_C. This may be caused by differences in the value of n. For the fcaEC model, n does not decrease as much as for the fEC model. This could mean that the anode affected the CPE in the fEC model to behave more like a Warburg element for high currents. This has also lead to changes in the Q-value. For the fcanEC model, the Q-value was smoother. Note that keeping n constant affects Q by forcing it to have a constant unit over all currents.

4.4 Model Comparison

Resistances cause voltage losses, and are therefore intrinsically connected. The GT model is unable to calculate the corresponding resistances in the EC model or the

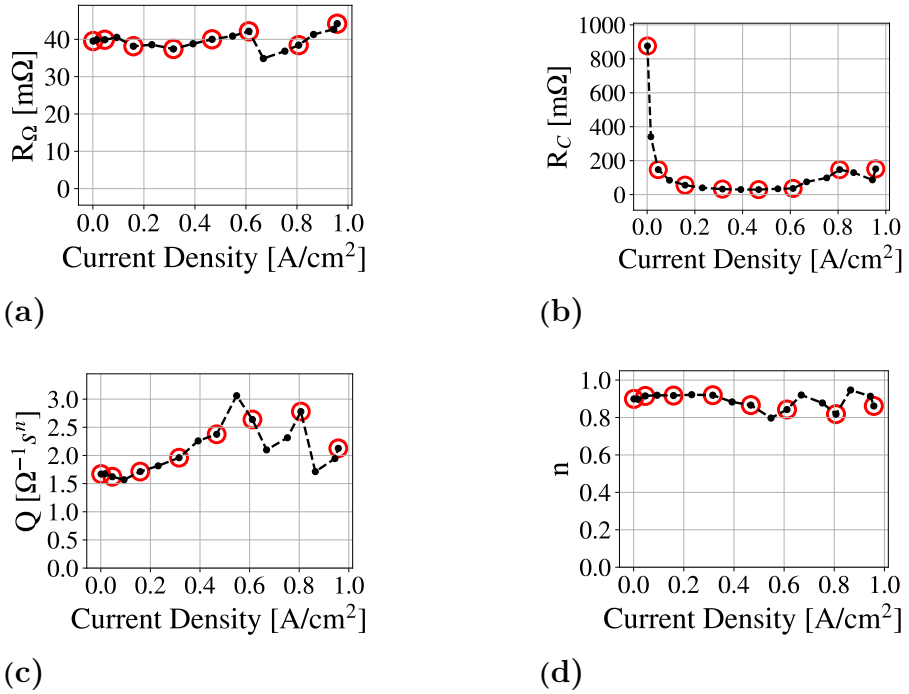

Figure 4.19: The electrical components in the fitted fcaEC model for experiment A. **(a)** is the ohmic resistance and **(b)** is the resistance of the parallel circuit representing the cathodic response. **(c)** and **(d)** are the CPE components of the same parallel circuit.

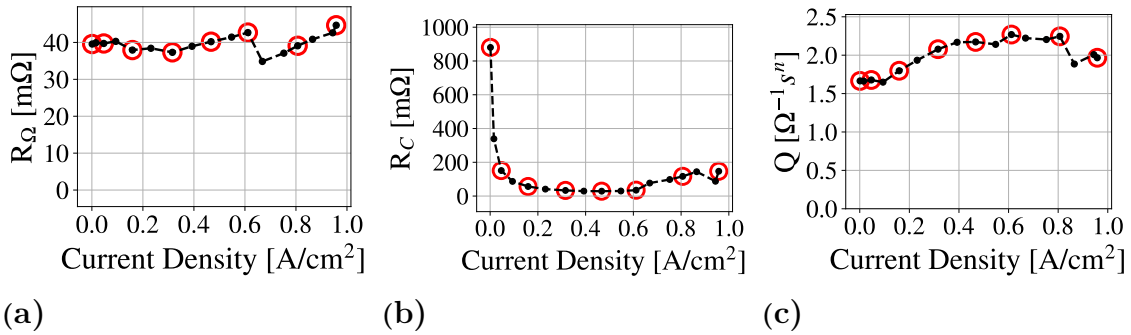

Figure 4.20: The electrical components in the fitted fcanEC model for experiment A. **(a)** is the ohmic resistance and **(b)** is the resistance of the parallel circuit representing the cathodic response. **(c)** represents the value of the non ideal capacitor in the CPE, where n is 0.9.

resistances of the components in the fuel cell (besides the membrane, which is later discussed). In order to connect the two models, a comparison between the resistances in the EC models presented in Figures 4.16, 4.17, 4.19 and 4.20, and the losses from the GT model presented in Figures 4.8 - 4.12 are made.

To start with, there is a strong connection between the ohmic losses calculated by the GT model and the EC model. The ohmic losses are linear. With Ohm's law,

this is what is expected for a constant resistance as can be seen for the ohmic resistance, R_Ω from the EC models. GT also calculated the ohmic resistance, R_{ohmic}, which is presented in Figure 4.21**a**. It is calculated by the correlations shown in (2.9) -(2.11). R_{ohmic} is relatively constant and the variation comes from variations in the membrane humidity which is presented in Figure 4.21**b**. The membrane humidity is modelled based on the inlet conditions and can deviate from the set 100% humidity. This is due to water transport phenomena in the membrane, as well as liquid water formation away from the membrane. It is therefore not simple to set the membrane humidity to a certain value such as 100%, as the water transport then needs to be balanced solely on achieving that value. Note that the membrane humidity in the GT fuel cell component is the average over the cathodic and the anodic sides of the membrane. All models resulted in 100% RH on the cathodic side of the membrane.

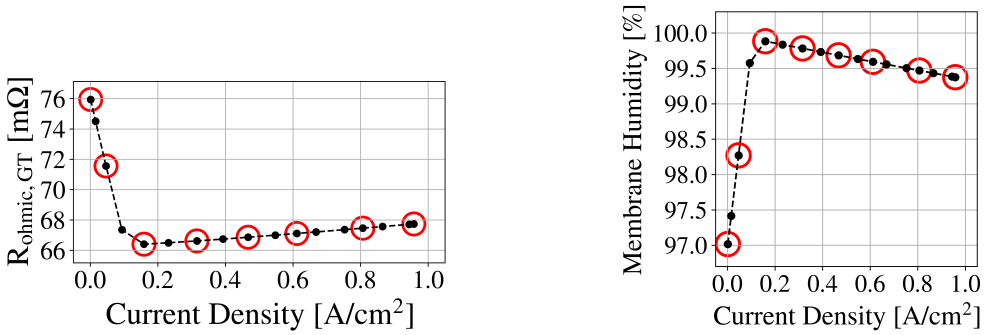

(a) **(b)**

Figure 4.21: The GT model results of **(a)** R_{ohmic} and **(b)** the membrane RH for experiment A using a constant porosity of 0.7. Red rings indicate the points used in the calibration.

The other models follow the same pattern as shown in Figure 4.21, where the membrane humidities increase to 100% RH to then slightly decrease at higher currents and are presented Appendix F. All models' maximum and minimum R_{ohmic} values are presented in Table 4.1 for the experiments presented in Table 3.1 excluding experiment B.3, due to problems related to the low humidity as previously described. As can be seen in Table 4.1, R_{ohmic} was overall measured to be higher than R_Ω from the fEC model (more than 50%), which can be seen from table 4.2. This indicates that the GT model overestimated the ohmic losses. This does not affect the polarisation curve for the calibrated state as it is fitted against the experimental data. However, it can become troublesome if different fuel cell configurations are compared. The results reveal that the distribution of losses cannot be trusted, which could result in that the wrong phenomena is optimised with lower impact on the performance than expected.
As described in section 2.6.2, R_Ω is the total ohmic resistance of the fuel cell. This resistance is mainly from the membrane, but also from the rest of the components and their contact resistances between each of them. If the components are not tightly packed, the contact worsens and the ohmic resistance increases. R_{ohmic} is

Table 4.1: The maximum and minimum values of R_{ohmic} for the different GT models calibrated for each experiment.

R_{ohmic}	Experiment A 80°C, 100% RH	Experiment B.1 80°C, 100% RH	Experiment B.2 40°C, 100% RH
Max [mΩ]	76	130	99
Min [mΩ]	66	106	90

Table 4.2: The constant value R_Ω from the fEC model for each experiment.

	Experiment A 80°C, 100% RH	Experiment B.1 80°C, 100% RH	Experiment B.2 40°C, 100% RH
$\sim$ R_Ω [mΩ]	40	70	50

defined from (2.9) - (2.11), i.e. only defined by the membrane resistance, but still results in a higher ohmic resistance than R_Ω. This indicates that the parameters can be wrongly tuned if based only on polarisation curve data.

As already mentioned, the total resistance (the low frequency intercept) of the fuel cell is the negative slope of the polarisation curve. For that reason, whether there is a connection between the slope of each voltage loss and the EC model resistances were investigated. The activation losses presented in section 4.2.3 increase for higher currents, with a high initial slope which then decreases for higher currents. In all EC models, the large semicircle is represented either by the charge transfer resistance, R_{Ct} or the cathodic resistance, R_C. The large semicircle is first large to then shrink with current. This is what is expected based on the literature for the activation region. The activation loss has a steep increase until a current density of $\sim$0.2 A/cm^2 as seen in Figure 4.8**a** for experiment A at a fixed porosity of 0.7. The resistances connected to the large semicircle (R_{Ct} and R_C) are seen to have a steep decline until the same current density is reached, as can be seen in Figures 4.16**c** and 4.17**d** respectively. The same pattern exists for the other experimental states, which is shown in Appendix G.

A similar connection can be made between concentration voltage losses and the resistances R_{Ct} and R_C. In Figures 4.16**c** and 4.17**d**, the resistances increase at higher currents. This could be an indication that the concentration losses affects the cell, but as seen in Figures 4.8 - 4.12, the concentration losses are negligible at the current voltage span and flow stoichiometry. From all EC models, it is unclear whether the concentration losses affected the cell. As seen from Figure 4.17**f**, n decreases in the fEC model at higher currents. This indicates that the CPE shifts toward an infinite Warburg response and would imply that the fuel cell is transitioning into the concentration region from the ohmic region. However, when the anode was set as constant, n stayed high at $\sim$0.9, and behaved like a non-ideal capacitor. Recall that the EIS data was unstable and noisy for higher currents, which complicates the interpretation further.

To conclude, there exists a relation between the ohmic resistance and the ohmic loss. The ohmic loss in the GT model could therefore be connected to the EC models' ohmic resistance. The calibration method in GT as of now overestimates the ohmic resistance. It is however unclear how to connect the activation and concentration losses to the EC models resistances, but there is a connection between them. This can be seen by that R_C and R_{Ct} are large at low currents concurrently with an increase in the activation loss from the GT model. R_C and R_{Ct} also increase at higher currents, which indicates an increase in concentration losses and a transition into the concentration region, but the loss is negligible.

5
Conclusions

The GT SUITE fuel cell tool has been illustrated using experimental data from a combined voltage stepping and EIS process of two different fuel cells. The calibration process of the GT model has been repeated for each operating condition and evaluated on its qualitative performance in comparison to expected behaviour from literature. The GT model reproduces polarisation curves well with only two calibration parameters for one state, one in the activation voltage loss and one in the membrane conductivity model, given that the experimental data never measures the concentration region. The GT model also predicts another temperature state that coincides with the literature.

The comparison of the voltage losses of the GT and equivalent circuit models show that the voltage losses and resistances are connected. Mainly, the ohmic resistance is shown to be connected by Ohm's law in the GT model, but that it is overestimated. Since an error in one voltage loss impacts the other voltage losses, it is shown that the voltage losses are not accurate as is. When the distribution of losses are important, e.g. when comparing or choosing between fuel cells, it could result in incorrect conclusions.

From this thesis result, GT SUITE is shown to be good at simulating the performance of the fuel cell with different states such as temperature and relative humidity. Caution is needed when using it for the fuel cell components contribution to the performance.

5.1 Future Work

Further investigations on implementing EIS data into the calibration process of the GT model of a fuel cell is needed. A suggested approach could be to include a residual that forces the ohmic loss parameters to follow the ohmic resistance from the EC model. With a larger data set, predictions might also be made of other states in GT. Models could also be based on combined states, similar to what was done in Section 4.2.2, but without degradation and the predictions could be made of interpolated states.

In the future, each physical phenomena in GT could be investigated further as well. The heat transfer modelling could be studied by introducing their built-in water

coolant channels in the fuel cell, depending on if that experimental data is supplied. The back pressure can be experimentally varied to see its effect on each voltage loss and equivalent circuit model parameter. The fuel cell's membrane humidity model could be further studied as well, specifically how it changes in validity when operating fuel cells with a different brand of membrane than Nafion.

Besides what is presented in the results, an investigation of the possibility to simulate an EIS experiment in GT SUITE was performed. The idea was to see the response from the GT fuel cell component, then use Fourier transform to find the phase difference between current and voltage similar to (2.14). This plan failed. Christian Altenhofen at GT informed us that at the current state, the GT model is not able to handle the fast frequencies of EIS. A hypothesis is that the measured phase shift in GT was strongly dependent on the time step size instead of the modelled electrochemical processes. As this approach did not work, it would be interesting to investigate how the GT model handles current and voltage step responses in the future, to see if it can handle the dynamics of the cell as well as the steady state results.

5.2 Sustainability Aspects

The project itself has little direct environmental impact, since it only entailed numerical simulations. However, the simulations were calibrated from experimental data. The experiments themselves required smaller amounts of hydrogen gas since they were performed on a single cell. The lab setup was built prior to the master thesis project for other applications, thus the environmental impact of the build itself is not connected to this thesis. The fuel cell itself was small (5 cm^2 geometric area) and the platinum loading was lower than typical values ($4 \cdot 10^{-4} mg/cm^2$ compared to 0.1 mg/cm^2 [40]), which lowers the environmental impact further.

This thesis aims at contributing to the development of fuel cells. As previously described in Section 1.1, fuel cells have the potential to complement batteries as a green alternative to fossil fuel based engines for long distance heavy duty vehicles. However, fuel cells' environmental impact are dependent on the production method of the hydrogen gas. It is either produced from natural gas or electrolysis, but electrolysis comes with a significant decrease in efficiency [41]. Implementation of PEM fuel cells would also require a large investment and expansion of a hydrogen infrastructure which comes with its own consequences. Fuel cells still require rare metals at this point in time, as well. Overall, researching PEM fuel cell modelling further has the possibility of lowering CO_2 emissions, dependent on factors that are difficult to predict.

5.3 Ethical Aspects

The simulations themselves have no potential to cause harm. However, there are always safety risks when running fuel cell experiments, specifically regarding hydrogen

gas (as briefly mentioned in Section 2.5). Since they were performed by experienced personnel at Chalmers in a sealed enclosure with safety precautions (such as hydrogen detectors and emergency exhausts), risks were minimised.

The fuel cell's environmental impact and ethical aspects are intertwined. Rare metal mining increase the risk of exploitative work under poor working conditions as they are operated today (such as development of lung diseases due to quartz particles exposure [42]). Unless efficient recycling of rare metals is on its way, it is also arguably unethical to develop green technologies that are dependent on a known depleting resource. Fuel cell development also replaces old occupations that could lead to layoffs. It could destabilise workers' economies unless re-education is readily available.

Bibliography

[1] Rupinder Singh, Amandeep Singh Oberoi, and Talwinder Singh. Factors influencing the performance of pem fuel cells: A review on performance parameters, water management, and cooling techniques. *International Journal of Energy Research*, 2021.

[2] Joeri Van Mierlo and Gaston Maggetto. Fuel cell or battery: Electric cars are the future. *Fuel Cells*, 7(2):165–173, 2007.

[3] Saeed Solaymani. Co2 emissions patterns in 7 top carbon emitter economies: the case of transport sector. *Energy*, 168:989–1001, 2019.

[4] Carlo Cunanan, Manh-Kien Tran, Youngwoo Lee, Shinghei Kwok, Vincent Leung, and Michael Fowler. A review of heavy-duty vehicle powertrain technologies: Diesel engine vehicles, battery electric vehicles, and hydrogen fuel cell electric vehicles. *Clean Technologies*, 3(2):474–489, 2021.

[5] A Ajanovic and R Haas. Economic and environmental prospects for battery electric-and fuel cell vehicles: a review. *Fuel cells*, 19(5):515–529, 2019.

[6] Zuraida Binti Awang Mat, Yap Boon Kar, Saiful Hasmady Bin Abu Hassan, Noor Azrina Binti Talik, et al. Proton exchange membrane (pem) and solid oxide (sofc) fuel cell based vehicles-a review. In *2017 2nd IEEE international conference on intelligent transportation engineering (ICITE)*, pages 123–126. IEEE, 2017.

[7] Ryan O'hayre, Suk-Won Cha, Whitney Colella, and Fritz B Prinz. *Fuel cell fundamentals*. John Wiley & Sons, 2016.

[8] Seyed Mohammad Rezaei Niya and Mina Hoorfar. Study of proton exchange membrane fuel cells using electrochemical impedance spectroscopy technique–a review. *Journal of Power Sources*, 240:281–293, 2013.

[9] T. E. Springer, T. A. Zawodzinski, and S. Gottesfeld. Polymer electrolyte fuel cell model. *Journal of The Electrochemical Society*, 138(8):2334–2342, aug 1991.

[10] Adam Z Weber and John Newman. Modeling transport in polymer-electrolyte fuel cells. *Chemical reviews*, 104(10):4679–4726, 2004.

[11] Xiao-Zi Yuan, Chaojie Song, Haijiang Wang, and Jiujun Zhang. Electrochemical impedance spectroscopy in pem fuel cells: fundamentals and applications. 2010.

[12] Kah Wai Lum and James Joseph McGuirk. Three-dimensional model of a complete polymer electrolyte membrane fuel cell – model formulation, validation and parametric studies. *Journal of Power Sources*, 143(1):103–124, 2005.

[13] A Bertei, E Ruiz-Trejo, F Tariq, V Yufit, A Atkinson, and NP Brandon. Validation of a physically-based solid oxide fuel cell anode model combining 3d tomography and impedance spectroscopy. *international journal of hydrogen energy*, 41(47):22381–22393, 2016.

[14] Gamma Technologies. Gt-suite, integrated multi-physics systems simulation. `www.gtisoft.com/gt-suite/`. Accessed: 2022-01-28.

[15] Frano Barbir and Frano Barbir. *PEM Fuel Cells : Theory and Practice.* Sustainable World. Elsevier Science & Technology, 2005.

[16] Annamalai Kirubakaran, Shailendra Jain, and RK Nema. A review on fuel cell technologies and power electronic interface. *Renewable and Sustainable Energy Reviews*, 13(9):2430–2440, 2009.

[17] Hao Wu. Mathematical modeling of transient transport phenomena in pem fuel cells. 2009.

[18] Tsotridis G, Pilenga A, De Marco G, and Malkow T. Eu harmonised test protocols for pemfc mea testing in single cell configuration for automotive applications. Technical Report LD-NA-27632-EN-C (print),LD-NA-27632-EN-N (online), Publications Office of the European Union, Luxembourg (Luxembourg), 2015.

[19] Yun Wang, Daniela Fernanda Ruiz Diaz, Ken S Chen, Zhe Wang, and Xavier Cordobes Adroher. Materials, technological status, and fundamentals of pem fuel cells–a review. *Materials Today*, 32:178–203, 2020.

[20] Yun Wang, Bongjin Seo, Bowen Wang, Nada Zamel, Kui Jiao, and Xavier Cordobes Adroher. Fundamentals, materials, and machine learning of polymer electrolyte membrane fuel cell technology. *Energy and AI*, 1:100014, 2020.

[21] Yun Wang, Ken S. Chen, and Sung Chan Cho. *PEM fuel cells: Thermal and Water Management Fundamentals*. Momentum Press, 2013.

[22] A. P. Young, J. Stumper, and E. Gyenge. Characterizing the structural degradation in a PEMFC cathode catalyst layer: Carbon corrosion. *Journal of The Electrochemical Society*, 156(8):B913, 2009.

[23] Natalia Macauley, Dennis D. Papadias, Joseph Fairweather, Dusan Spernjak, David Langlois, Rajesh Ahluwalia, Karren L. More, Rangachary Mukundan, and Rodney L. Borup. Carbon corrosion in PEM fuel cells and the development of accelerated stress tests. *Journal of The Electrochemical Society*, 165(6):F3148–F3160, 2018.

[24] Zhixiang Liu, Lizhai Yang, Zongqiang Mao, Weilin Zhuge, Yangjun Zhang, and Lisheng Wang. Behavior of pemfc in starvation. *Journal of Power Sources*, 157(1):166–176, 2006.

[25] Allen J. Bard and Larry R. Faulkner. *Electrochemical Methods*. John Wilen & Sons, 2001.

[26] J Ross Macdonald and Evgenij Barsoukov. *Impedance spectroscopy: theory, experiment, and applications*. John Wiley & Sons, 2018.

[27] Aparna M Dhirde, Nilesh V Dale, Hossein Salehfar, Michael D Mann, and Tae-Hee Han. Equivalent electric circuit modeling and performance analysis of a pem fuel cell stack using impedance spectroscopy. *IEEE transactions on energy conversion*, 25(3):778–786, 2010.

[28] Jinfeng Wu, Xiao Zi Yuan, Haijiang Wang, Mauricio Blanco, Jonathan J. Martin, and Jiujun Zhang. Diagnostic tools in pem fuel cell research: Part i electrochemical techniques. *International Journal of Hydrogen Energy*, 33(6):1735–1746, 2008.

[29] Dimiter N Petsev, Frank van Swol, and Laura J D Frink. *Molecular Theory of Electric Double Layers*. 2053-2563. IOP Publishing, 2021.

[30] Jordy Santana, Mayken Espinoza-Andaluz, Tingshuai Li, and Martin Andersson. A detailed analysis of internal resistance of a pefc comparing high and low humidification of the reactant gases. *Frontiers in Energy Research*, page 217, 2020.

[31] Uwe Beuscher, Simon J. C. Cleghorn, and William B. Johnson. Challenges for pem fuel cell membranes. *International Journal of Energy Research*, 29(12):1103–1112, 2005.

[32] Xinhuai Ye and Chao-Yang Wang. Measurement of water transport properties through membrane-electrode assemblies. *Journal of The Electrochemical Society*, 154(7):B676, 2007.

[33] Qiangu Yan, H. Toghiani, and Heath Causey. Steady state and dynamic performance of proton exchange membrane fuel cells (pemfcs) under various operating conditions and load changes. *Journal of Power Sources*, 161(1):492–502, 2006.

[34] Christoph Hartnig, Ingo Manke, Robert Kuhn, Sebastian Kleinau, Jürgen Goebbels, and John Banhart. High-resolution in-plane investigation of the water evolution and transport in pem fuel cells. *Journal of Power Sources*, 188(2):468–474, 2009.

[35] Hsin-Sen Chu, Chung Yeh, and Falin Chen. Effects of porosity change of gas diffuser on performance of proton exchange membrane fuel cell. *Journal of Power Sources*, 123(1):1–9, 2003.

[36] Andrea Ramírez-Cruzado, Blanca Ramírez-Peña, Rosario Vélez-García, Alfredo Iranzo, and José Guerra. Experimental analysis of the performance and load cycling of a polymer electrolyte membrane fuel cell. *Processes*, 8(5), 2020.

[37] Jay Benziger, E. Chia, J.F. Moxley, and I.G. Kevrekidis. The dynamic response of pem fuel cells to changes in load. *Chemical Engineering Science*, 60(6):1743–1759, 2005.

[38] Saurabh A. Vilekar and Ravindra Datta. The effect of hydrogen crossover on open-circuit voltage in polymer electrolyte membrane fuel cells. *Journal of Power Sources*, 195(8):2241–2247, 2010.

[39] M.G. Santarelli, M.F. Torchio, and P. Cochis. Parameters estimation of a pem fuel cell polarization curve and analysis of their behavior with temperature. *Journal of Power Sources*, 159(2):824–835, 2006.

[40] Anusorn Kongkanand and Mark F. Mathias. The priority and challenge of high-power performance of low-platinum proton-exchange membrane fuel cells. *The Journal of Physical Chemistry Letters*, 7(7):1127–1137, 2016. PMID: 26961326.

[41] S. Shiva Kumar and V. Himabindu. Hydrogen production by pem water electrolysis – a review. *Materials Science for Energy Technologies*, 2(3):442–454, 2019.

[42] Maasago M Sepadi, Martha Chadyiwa, and Vusumuzi Nkosi. Platinum mine workers' exposure to dust particles emitted at mine waste rock crusher plants in limpopo, south africa. *International journal of environmental research and public health*, 17(2):655, 2020.

[43] Dortmund data bank (ddb). `http://ddbonline.ddbst.com/AntoineCalculation/AntoineCalculationCGI.exe`. Accessed: 2022-05-18.

A

Appendix: Physical Properties and Simulation Parameters

Physical properties of the fuel cells and simulation parameters for the GT models are listen below.

Table A.1: Fuel cell properties.

Geometry	
Geometric area	5 cm^2
Flow pattern	single serpentine
total weight	132 g

Table A.2: Electrode properties.

Electrodes	
Catalyst loading	$4 \cdot 10^{-4}$ mg/cm^2
GDL thickness	280 μm
GDL tortuosity	1.6

Table A.3: Fuel cell membrane properties for both fuel cells.

Membrane	
Membrane thickness	50.8 μm
dry density	2000 kg/m^3
dry equivalent weight	1100 g/mol

Table A.4: Simulation parameters. Values presented by themselves are constant for both flexible and fixed porosity. Values presented with "/" between are dependent of porosity (fixed/flexible porosity). Experiment B.2 was not calibrated with genetic algorithm for the porosity.

	Fuel cell A: 80 °C, 100% RH	Fuel cell B: 80 °C, 100% RH	Fuel cell B: 40 °C, 100% RH
k_{OCV} [mV]	36	54	50
σ_{11} $[(\Omega\text{cm})^{-1}]$	9.33E-4/ 8.39E-4	7.64E-4/ 7.83E-4	9.37E-4/ -
α	0.754/ 0.806	0.853/ 0.826	0.774/ -
fixed/ flexible porosity	0.7/ 0.97	0.7/ 0.55	0.7/ -
Reference ECD per geom. surface area [A/cm^2]	6.342E-9	6.342E-9	6.342E-9

Table A.5: Simulation parameters for the combined model.

	Fuel cell B: combined 80 & 40 C, 100% RH
k_{OCV} [mV]	50
σ_{11} $[(\Omega\text{cm})^{-1}]$	9.37E-4
α	0.774
porosity	0.7
Reference ECD per geom. surface area [A/cm^2]	6.342 E-9

B

Appendix: Stoichiometry Calculation

The lowest reactant stoichiometry was calculated based on the highest measured DC current over fuel cell A at 100% RH at atmospheric pressure ($P = 101325$ Pa). Antoine equation parameter values can be found at the online Dortmund Data bank [43].

$$log_{10}\left(\frac{P_{sat}[Pa]}{133.32[\text{Pa/mmHg}]}\right) = \frac{A-B}{C+T[^\circ C]} \tag{B.1}$$

$$A = 8.07131, B = 1730.63, C = 233.426 \tag{B.2}$$

$$P_{sat} = 133.32 \cdot 10^{(A-B)/(C+T)} = \begin{cases} 7358.4 \text{ [Pa] for } 40^\circ\text{C} \\ 47267 \text{ [Pa] for } 80^\circ\text{C} \end{cases} \tag{B.3}$$

$$y_v = \frac{RH \cdot P_{sat}}{P} = \begin{cases} 0.0719 \text{ for } 40^\circ\text{C} \\ 0.4618 \text{ for } 80^\circ\text{C} \end{cases} \tag{B.4}$$

The total molar flow rate at the anode ($n_{tot,A}$) was calculated with the assumption of an ideal gas mix, based on the given volumetric flow rate of 0.14 L/min (or 2.33E-6 m^3/s) on the anode inlet (V_A) and 0.4 L/min (or 6.67E-6 m^3/s) on the cathode inlet (V_C).

$$n_{tot,A} = \frac{V_A[\text{m}^3/\text{s}] \cdot P[\text{Pa}]}{R[\text{J/molK}] \cdot T[\text{K}]} = \frac{\text{2.33E-6} \cdot 101325}{8.3144 \cdot T} = \begin{cases} \text{9.1E-5 mol/s for } 40^\circ\text{C} \\ \text{8.0E-5 mol/s for } 80^\circ\text{C} \end{cases} \tag{B.5}$$

The molar flow rate at the cathode ($n_{tot,C}$) is solved the same way.

$$n_{tot,C} = \frac{V_C P}{RT} = \begin{cases} \text{2.6E-4 mol/s for } 40^\circ\text{C} \\ \text{2.3E-4 mol/s for } 80^\circ\text{C} \end{cases} \tag{B.6}$$

The lowest stoichiometric factor S is at the highest current of 5 A for fuel cell A.

$$S_{O_2} = \frac{4n_{O_2}F}{I} = \frac{4 \cdot 0.233(1-y_v)n_{tot,C} \cdot 96485.3}{5} = \begin{cases} 4.3 \text{ for } 40^\circ\text{C} \\ 2.2 \text{ for } 80^\circ\text{C} \end{cases} \tag{B.7}$$

$$S_{H_2} = \frac{2n_{H_2}F}{I} = \frac{2 \cdot 0.233(1-y_v)n_{tot,A} \cdot 96485.3}{5} = \begin{cases} 3.2 \text{ for } 40^\circ\text{C} \\ 1.7 \text{ for } 80^\circ\text{C} \end{cases} \tag{B.8}$$

where S_{H_2} is the hydrogen stoichiometric factor for HOR and S_{O_2} is the oxygen stoichiometric factor for ORR. These factors are within limits of a functioning fuel cell.

C

Appendix: Transient Behaviour

The transient behaviour of fuel cell B is presented for experiments B.1, B.2 and B.3 in Figures C.1, C.2 and C.3 respectively. As mentioned, these show similar behaviours as experiment A in Figure 4.1. They have droplets and become more unstable for higher currents. The red rings are incorporated for experiment B in the same way as in experiment A to visualise the chosen points for the calibration of the GT model. They also work as an indication of the most stable points, where a distribution of points over the whole current span is represented. As mentioned before, a GT model based on experiment B.3 was not successfully implemented, therefore no red rings are visualised in Figure C.3.

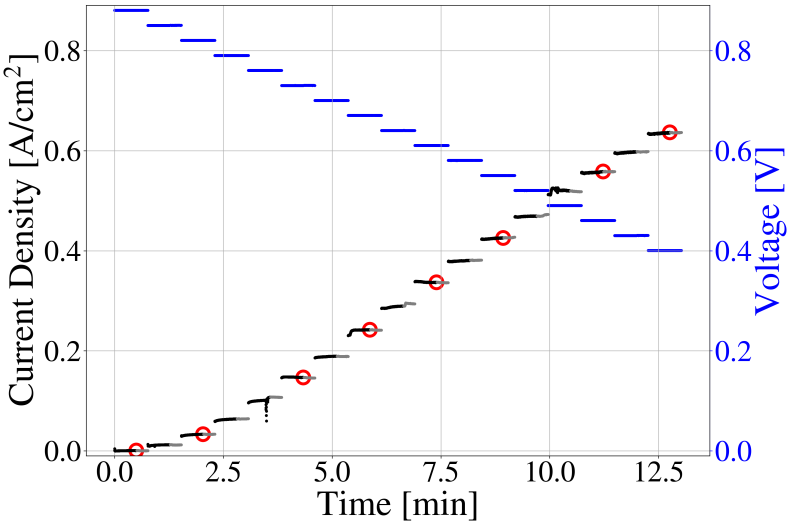

Figure C.1: Transient data for fuel cell B.1 at 80 °C, 100% RH.

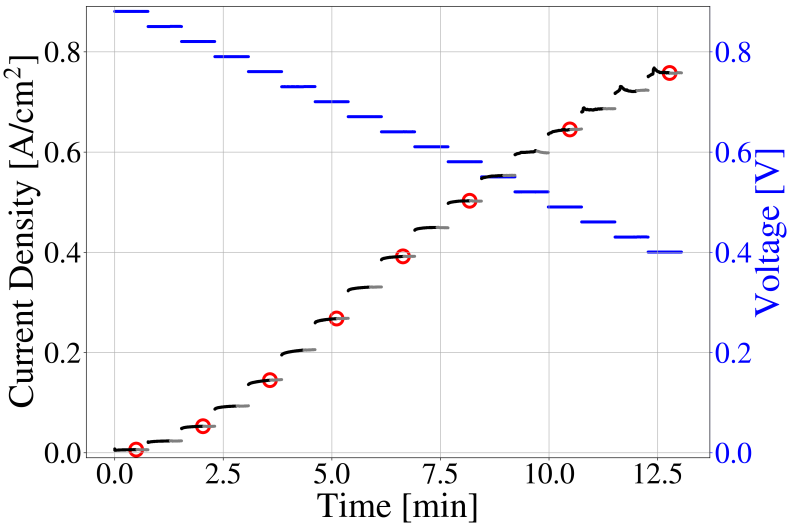

Figure C.2: Transient data for fuel cell B.2 at 40 °C, 100% RH.

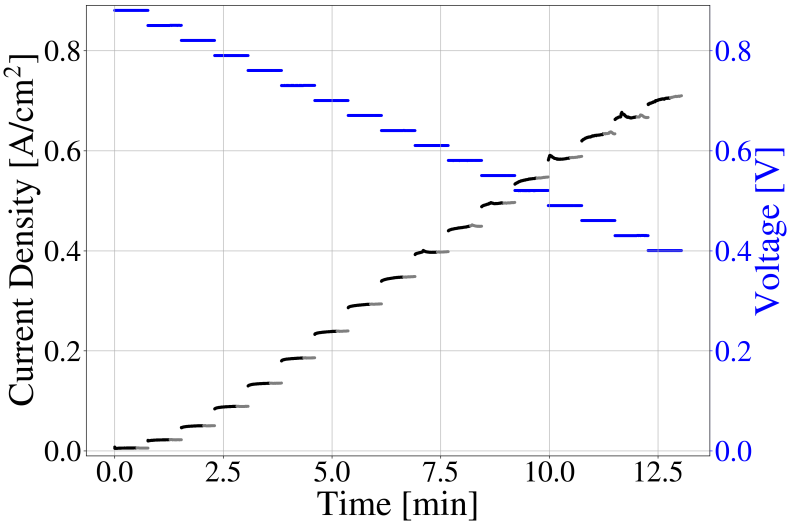

Figure C.3: Transient data for fuel cell B.3 at 40 °C, 41% RH.

D

Appendix: Impact of Porosity

Figure D.1 shows no deviation in calibration (polarisation curve) from setting the porosity fixed to 0.7 as in D.1**b** or using the genetic algorithm as in Figure D.1**a** for experiment B.1.

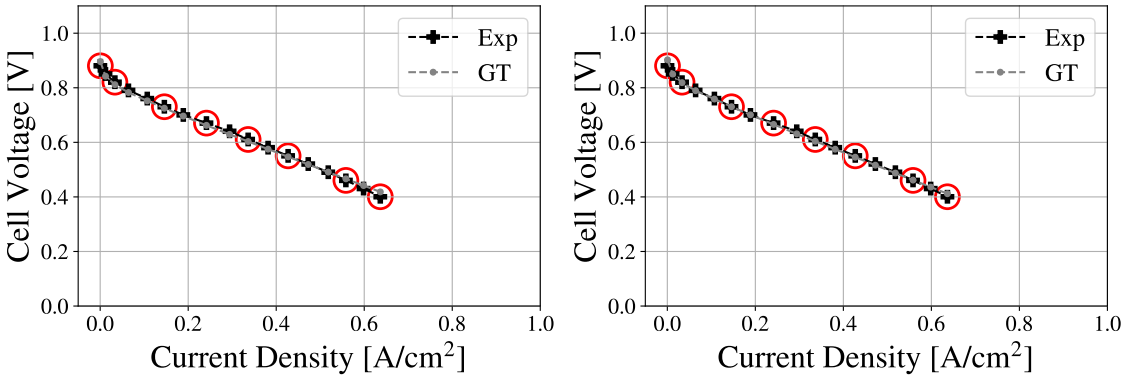

(a) **(b)**

Figure D.1: Calibration of experiment B.1 at 80 °C, 100% RH at both inlets (anode and cathode). Black line indicates the experimental data and grey line show the result from the GT model. Red circles mark the points that the model used to calibrate the model. In **(a)** the porosity set during calibration by the genetic algorithm was 0.55 and in **(b)** the porosity was fixed to 0.7.

However, as seen in Figures D.2 and D.3 there are differences in how the losses are distributed, but as mentioned before the concentration loss is negligible. Similarly to experiment A, the conclusion can be drawn that the porosity can be fixed, hence both fuel cell A and B used fixed porosity of 0.7 in the report.

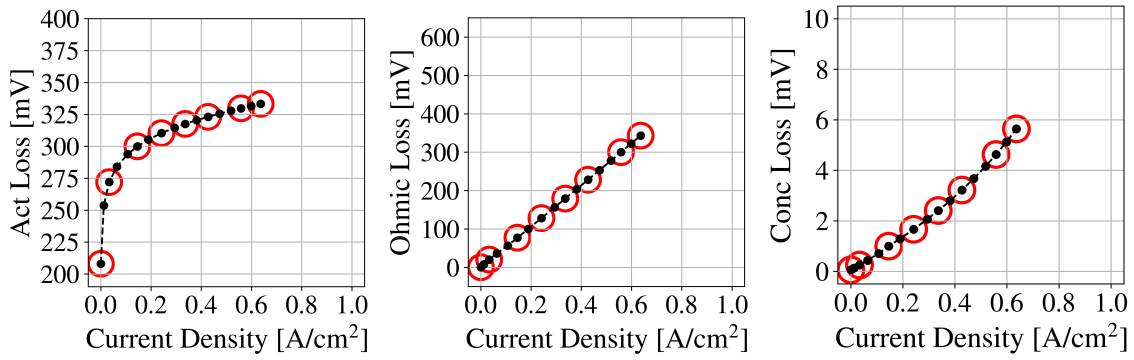

(a) (b) (c)

Figure D.2: Modelled voltage losses for experiment B.1 in GT at 80 °C, 100 RH with porosity 0.55.

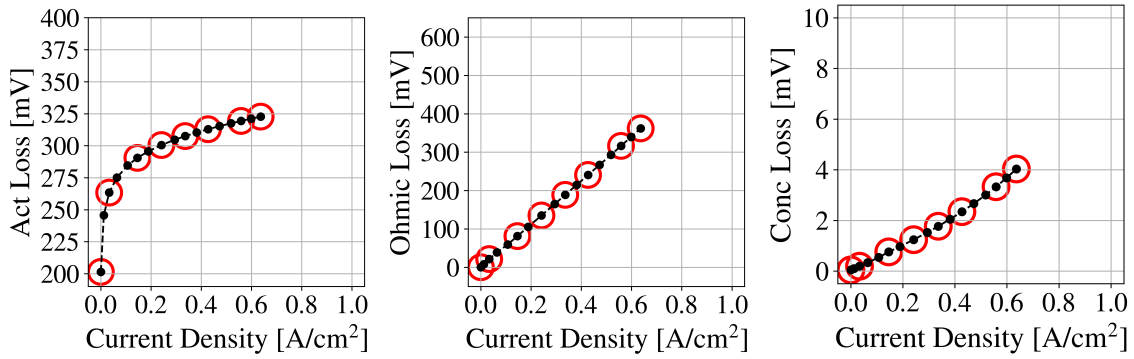

(a) (b) (c)

Figure D.3: Modelled voltage losses for experiment B.1 in GT at 80 °C, 100 RH with fixed porosity 0.7.

E

Appendix: Fitting of New EC Models

Here, additional Nyquist curves show the fitting of the fcaEC model and the fcanEC model in Figures E.1 and E.2 respectively.

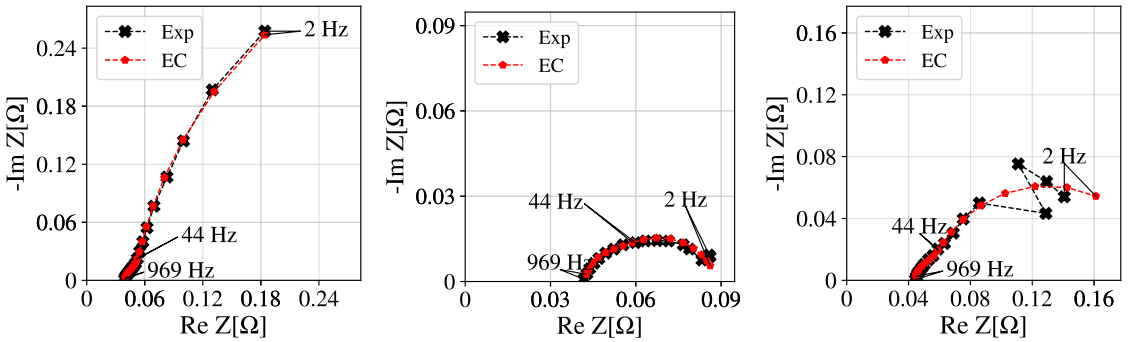

(a) 1.2 mA/cm^2 **(b)** 480 mA/cm^2 **(c)** 960 mA/cm^2

Figure E.1: Nyquist curves for the experimental (EIS) data A as black crosses and the flexible EC model with constant anode as red dots. The EC model with constant anode is fitted with non-linear least squares and the frequency spans between 2Hz to ∼1kHz.

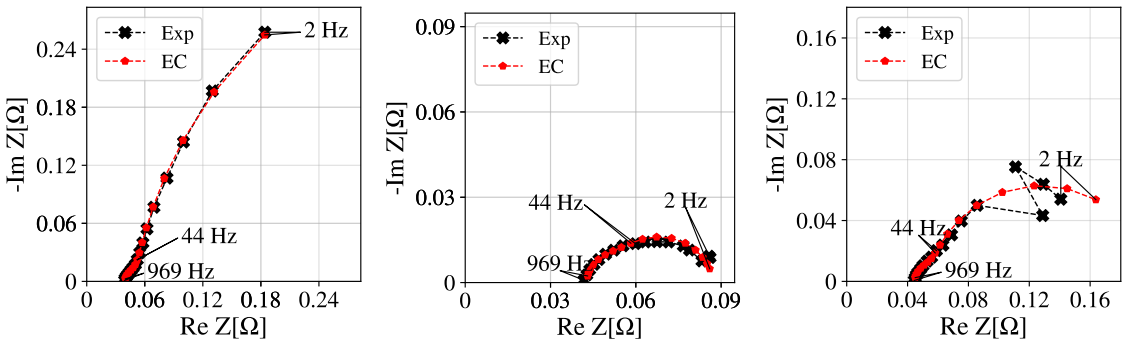

(a) 1.2 mA/cm^2 **(b)** 480 mA/cm^2 **(c)** 960 mA/cm^2

Figure E.2: Nyquist curves for the experimental (EIS) data A as black crosses and the flexible EC model with constant anode and n as red dots. The EC model with constant anode and n is fitted with non-linear least squares and the frequency spans between 2Hz to ∼1kHz.

F

Appendix: Ohmic Resistance and Membrane Humidity

R_{ohmic} from the GT models based on experiments B.1 and B.2 are presented in Figures F.1 and F.2 respectively. RH show the same pattern as for experiment A in the report thereby also R_{ohmic}.

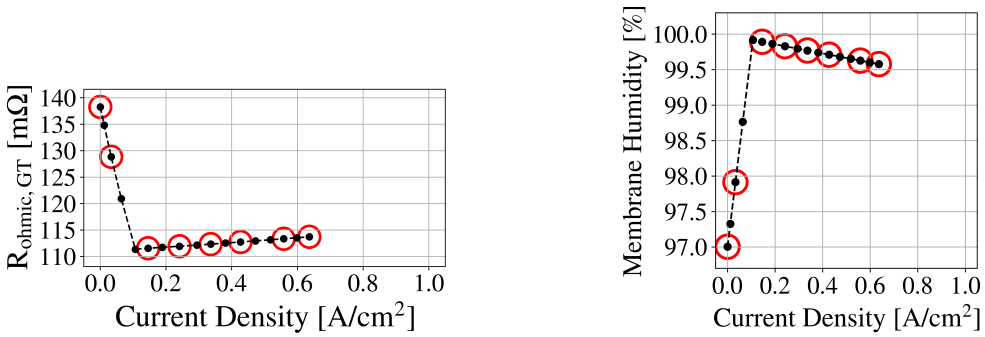

(a) **(b)**

Figure F.1: In **(a)** R_{ohmic} calculated with the GT model for experiment B at a temperature of 80°C and relative humidity of 100%. In **(b)** the membrane humidity in the same model. Red rings indicate the points used in the calibration.

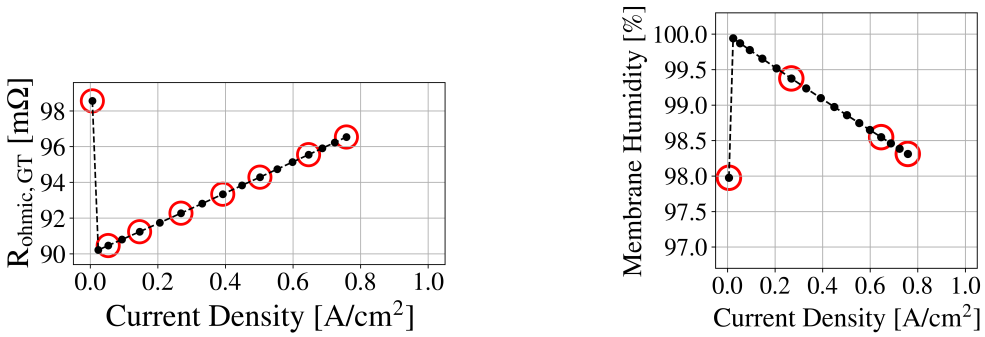

(a) **(b)**

Figure F.2: In **(a)** R_{ohmic} calculated with the GT model for experiment B at a temperature of 40°C and relative humidity of 100%. In **(b)** the membrane humidity in the same model. Red rings indicate the points used in the calibration.

G

Appendix: Connection Between Losses and Cathodic Resistance

Visualisation of the connection between activation loss and concentration loss, and the EC model in Figures G.1 and G.2. The EC model shown in Figures G.1**b** and G.2**b** is the flexible EC model. Similar to what is said in the report for experiment A, there is also a connection for experiment B as can be seen for the activation loss slope. It is large for low currents as seen in Figures G.1**a** and G.2**a** to then decrease at ~ 0.2 A/cm^2 and then stagnant. It is the same that happens with R_C, but instead of the slope the value of R_C. There is also an increase for R_C towards higher currents, which could be caused by transitioning into concentration region and the increase of concentration losses.

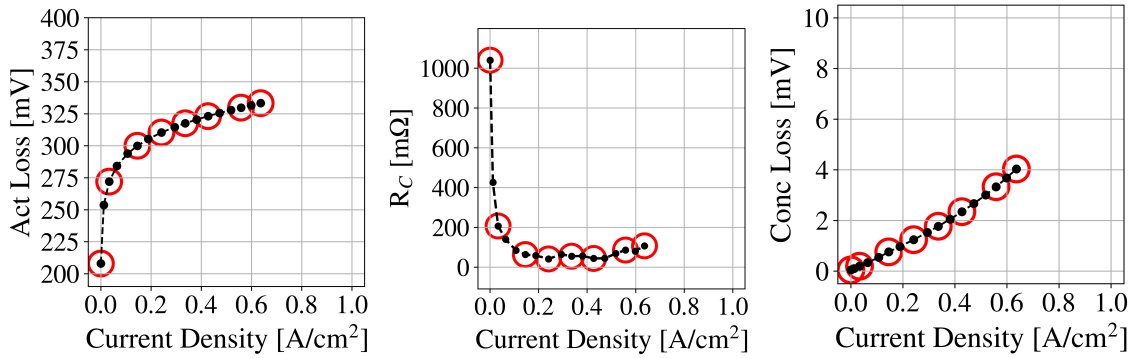

(a) **(b)** **(c)**

Figure G.1: The GT model losses and the EC model cathodic resistance for experiment B.1. In **(a)** and **(c)** the activation and concentration losses respectively. In **(b)** the flexible EC model.

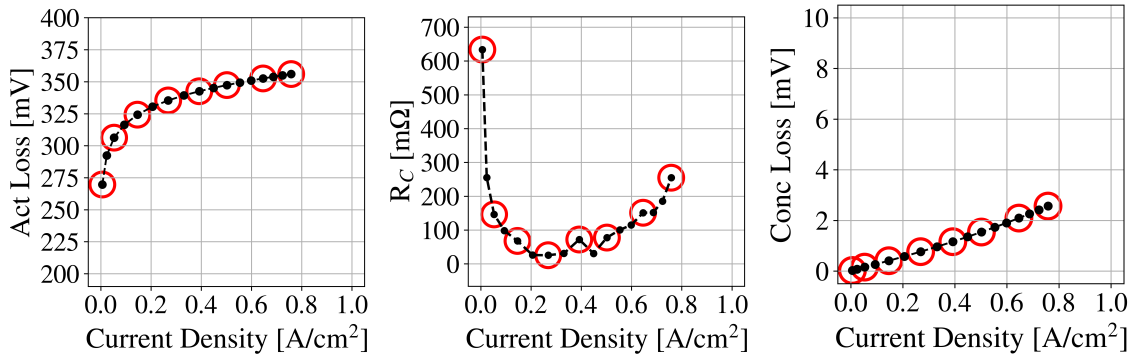

(a) **(b)** **(c)**

Figure G.2: The GT model losses and the EC model cathodic resistance for experiment B.2. In **(a)** and **(c)** the activation and concentration losses respectively. In **(b)** the flexible EC model.

DEPARTMENT OF ELECTRICAL ENGINEERING
CHALMERS UNIVERSITY OF TECHNOLOGY
Gothenburg, Sweden
www.chalmers.se

CHALMERS
UNIVERSITY OF TECHNOLOGY